Generalizable Modelling of Vacuum-Powered Soft Actuators

And Its Use in Design for Mechanical Assistive Applications

by

Samuel Dutra Gollob

B.S., University of Maryland, College Park (2019)

Submitted to the Department of Mechanical Engineering
in partial fulfillment of the requirements for the degree of

Master of Science in Mechanical Engineering

at the

MASSACHUSETTS INSTITUTE OF TECHNOLOGY

June 2021

Author . . . . . .
Department of Mechanical Engineering
May 14, 2021

Certified by . . . . . .
Ellen Roche
Associate Professor, Department of Mechanical Engineering and Institute for Medical Engineering and Science
Thesis Supervisor

Accepted by . . . . . .
Nicolas Hadjiconstantinou
Professor, Graduate Officer

Generalizable Modelling of Vacuum-Powered Soft Actuators And Its Use in Design for Mechanical Assistive Applications

by

Samuel Dutra Gollob

Submitted to the Department of Mechanical Engineering
on May 14, 2021, in partial fulfillment of the
requirements for the degree of
Master of Science in Mechanical Engineering

Abstract

In this thesis, we present a generalized modeling tool for predicting the output force profile of vacuum-powered soft actuators using a simplified geometrical approach and the principle of virtual work. Previous work has derived analytical formulas to model the force-contraction profile of specific actuators. To enhance the versatility and the efficiency of the modelling process we propose a generalized numerical algorithm based purely on geometrical inputs, which can be tailored to the desired actuator, to estimate its force-contraction profile quickly and for any combination of varying geometrical parameters. We identify a class of linearly contracting vacuum actuators that consists of a polymeric skin guided by a rigid skeleton and apply our model to two such actuators - vacuum bellows and Fluid-driven Origami-inspired Artificial Muscles (FOAMs) - to demonstrate the versatility of our model. We perform experiments to validate that our model can predict the force profile of the actuators using its geometric principles, modularly combined with design-specific external adjustment factors. Our framework can be used as a versatile design tool that allows users to perform parametric studies and rapidly and efficiently tune actuator dimensions to produce a force-contraction profile to meet their needs, and as a pre-screening tool to obviate the need for multiple rounds of time-intensive actuator fabrication and testing.

The work presented here was published in Frontiers in Robotics and AI on 03 March 2021, "A Modular Geometrical Framework for Modelling the Force-Contraction Profile of Vacuum-Powered Soft Actuators," by S. Gollob et al. [1] Figures reproduced from this work are referenced following the journal's open-access Creative Commons practices.

Thesis Supervisor: Ellen Roche
Title: Associate Professor, Department of Mechanical Engineering and Institute for Medical Engineering and Science

Acknowledgments

Before the traditional acknowledgement of those who have been essential for my completion of this work, I would be remiss not to note the year of this document is written in. Much of the work included in this thesis was completed during the COVID-19 global pandemic, which saw the lives of every human on the planet disrupted in significant ways – in the best of cases. It has changed the way I view and value my work, my position in the world, and my contact with other people. I start with a simple acknowledgement – in the neutral sense of the word – of what I and we all have lived for over a year.

I would like to acknowledge my advisor, Dr. Ellen Roche, for all her input and guidance in developing this work. Beyond this, she has provided me with support and opportunities throughout my Master's, to allow me to explore my various interests in the field of soft robotics and beyond, as I make my path towards my PhD studies. I have grown over the past two years as a researcher, and this has been in large part due to Ellen's guidance and support.

I would also like to thank my colleagues at the TTDD Lab at MIT, especially Clara Park and Brandon Koo for their help throughout the execution of this work, and Claudia Varela and Lucy Hu for their meaningful mentorship before and during my graduate studies. Thank you to Dr. Emir Vela and Mijaíl Mendoza Flores at UTEC, Perú, as our collaborators for help in continually developing a practical application for the work in this thesis.

Dr. Sarah Bergbreiter, Dr. Ryan St. Pierre, and Dr. Elizabeth Smela have introduced me to research during my undergraduate studies, and I am thankful for the opportunities and lessons they have provided me.

Last but certainly not least, I would like to thank my parents, Dr. Kenneth Gollob and Dr. Walderez Dutra for providing me with constant inspiration to pursue my studies as far as they will take me, to value the search for knowledge and the development of science, and for the constant guidance and support they have provided me through this journey. I also thank all my family in Brazil and the U.S. for their encouragement and love.

Contents

List of Figures

Chapter 1

Introduction

Soft robotics is a growing field, owing somewhat to an increasing demand for machines that can interact more safely with humans and their environment, generate complex multi-degree-of-freedom motions, and resist impact damage [2]. The sub-field of soft artificial muscles is relevant to the field of soft robotics as whole and will be the focus of this thesis, as they are commonly used to actuate soft robots as opposed to traditional motors. Although a variety of artificial muscle actuation schemes have been developed, including shape-memory alloys [3], tension cables [4], and phase transitions [5], fluidic actuation is widely used, as it is compatible with soft matrices, with programmed fluidic channels, and provides a means to change actuator volume and effective stiffness analogous with the contraction and stiffening of biological muscle [2]. Pneumatic artificial muscles have been used in, and theorized for, a range of applications, from medical implantable devices[6, 7], to exoskeletons[8, 9], and both soft and rigid robotic applications[10].

Most soft pneumatic actuators described in the literature operate with positive pressure, often involving a section of the actuator which expands with pressure and a strain-limiting component which guides the elastic expansion in a desired direction. This duality has been achieved by creating geometrical asymmetry in elastomeric actuators [11, 12], introducing an off-axis strain-limiting material for bending motions [13, 14], and reinforcing the outer skin of the actuator with fibers[15, 16, 17, 18]. Although positive pressure actuators can produce complex motions and large forces [2], they have limited contraction ratios, high actuation pressure requirements, and are subject to delamination or bursting[18, 19, 20, 21].

Owing to their dependence on volume increase for contraction, they pose a design challenge for applications where space is constrained.

Vacuum-operated soft pneumatic actuators are an alternative to positive pressure actuators that can avoid some of these pitfalls, while still achieving similar bending [22, 23], linear[24, 25, 21, 26, 27, 28], and complex programmed motions[29, 21]. This class of actuators rely on a decreasing volume for actuation, in contrast to positive pressure actuators where the volume typically increases upon actuation. Similar to the strain-limiting operating principle for positive pressure actuators, vacuum actuators often involve a thin strain-limited "skin" that is responsible for a decrease in volume upon actuation, and a "skeleton" that limits compression to guide the volume decrease in a desired direction [22, 21, 28, 27]. In this work, this type of vacuum actuator will be referred to as a "skin-skeleton vacuum actuator." Particularly, this work focuses on skin-skeleton actuators that undergo linear contraction upon actuation. This class of actuators has achieved contraction ratios near or above 90%, is often lightweight, fast-moving, and resistant over many cycles, requires low actuation pressures, and produces a high power to weight ratio compared to positive pressure actuators [22, 21, 28, 27]. As a result of these design features, these actuators have potential benefit for a variety of applications, especially those requiring large linear displacement which is challenging to achieve with commonly reported artificial muscles.

Previous work has developed a variety of actuator models, often based on the Finite Element Method (FEM), for describing their actuator designs [30, 31, 32, 33]. These models allow in-depth characterization of corresponding actuators, predicting buckling modes, stress distributions and actuator motion as a function of pressure, expected force output, and cycle lifetime. FEM approaches have been shown to characterize actuators for their use in a particular application and maintain the versatility of their design for other applications – for example Nguyen Zhang (2020)[32] characterize a family of modular cells using FEM that can be combined for curling, linear, and twisting motions as desired by the end user. Though FEM models are successful in describing actuator performance in detail, their complexity means they are not ideal for higher-level design iterations and selection of broad design spaces for performance constraints. To our knowledge, a generalized, versa-

tile model that can rapidly generate information on an actuator's output is missing in the existing body of work. Such a model could be used before the time-consuming prototyping, material testing, and FEM model creation that comes with a more developed design.

Inspired by previous literature, in this thesis I will describe a developed model that makes use of the virtual work principle to extract an actuator's force-contraction output force based on its volume loss rate. This is implemented via a simple and versatile numerical algorithm using solely geometrical features of the actuator, such that it can be set up and solved orders of magnitude more rapidly than an FEM approach. The model can then overlay other components of the actuator – such as an intrinsic restoring force – to better approximate its force output. The force-contraction profile (FCP) is a common characterization metric to describe the actuator output force over the course of its contraction assuming a constant pressure, and it is nonlinear for most vacuum actuators. This nonlinearity creates demand for tools that can allow one to understand and predict the FCP for a given actuator design. There have been a variety of simplified models that attempt to predict such profiles. While some models make use of force balancing analytical and numerical finite element models [33, 21], others have modelled actuator outputs using analytical solutions to the principle of virtual work [18, 21, 27, 28], which allows a force profile to be estimated solely from the actuator's geometry:

$$F = P * \frac{dV}{ds} \tag{1.1}$$

Where V is the actuator's internal volume, P is the actuation pressure (usually assumed constant), and s is the contraction or current length of the actuator. Assuming no energy loss and an inextensible skin, the output of the virtual work equation (Equation (1)) can be used to estimate the force output of the actuator directly [21, 18]. The models based on the principle of virtual work mentioned above apply an analytical solution derived from the design and geometry of the actuator in question, following a typical workflow: a skin geometry is defined, used to derive a formula for volume as a function of contraction, and the volume formula is differentiated. In one instance, this analytical approach was combined with a minimizing function [27] to allow for the skin to change in cross-sectional

geometry to mimic the physical tendency to minimize volume in a vacuum.

In this work, we expand the use of the virtual work concept and present a generalized platform that enables rapid prediction of the FCP of a linearly contracting skin-skeleton vacuum actuator for any skin or skeleton geometry. By implementing a numerical approach in MATLAB (MathWorks), we create a versatile model that can be applied to different actuator designs, without the need for the development of a separate analytical model for each design. To demonstrate the application and capabilities of the framework, we use it to model the FCPs of two representative types of linear skin-skeleton actuators: the bellows actuators [27](Figure 1-1A), and the Fluid-driven Origami-inspired Artificial Muscles (FOAMs) [21] (Figure 1-1B). The bellows actuator was chosen for its simple design and pre-existing modelling work, and the FOAM was chosen because its semi-rigid zigzag shaped skeleton adds geometrical complexity and behaves like a spring, adding an additional restoring force component to test the framework's modularity. To validate the framework, we experimentally characterize Bellows and FOAMs actuators with varying geometric parameters and compare the experimental FCPs with those derived from the model. Finally, from the validated model, we perform a simple case study of how the actuator FCP can be used in an engineering design scenario and compare the outputs of this "virtual work model" and an FEM model in predicting application-specific parameters of control pressure. From this work, we seek to show that this Virtual Work model – despite limitations sprouting from its simplicity – has potential utility as a design tool for soft roboticists, or device designers, by allowing rapid exploration of a design space through its easy application to various actuator designs and geometries. Beyond its applicability, I hope this work can demonstrate the value of understanding the concept of virtual work, and keeping it in mind when considering new and existing designs of vacuum-powered soft actuators.

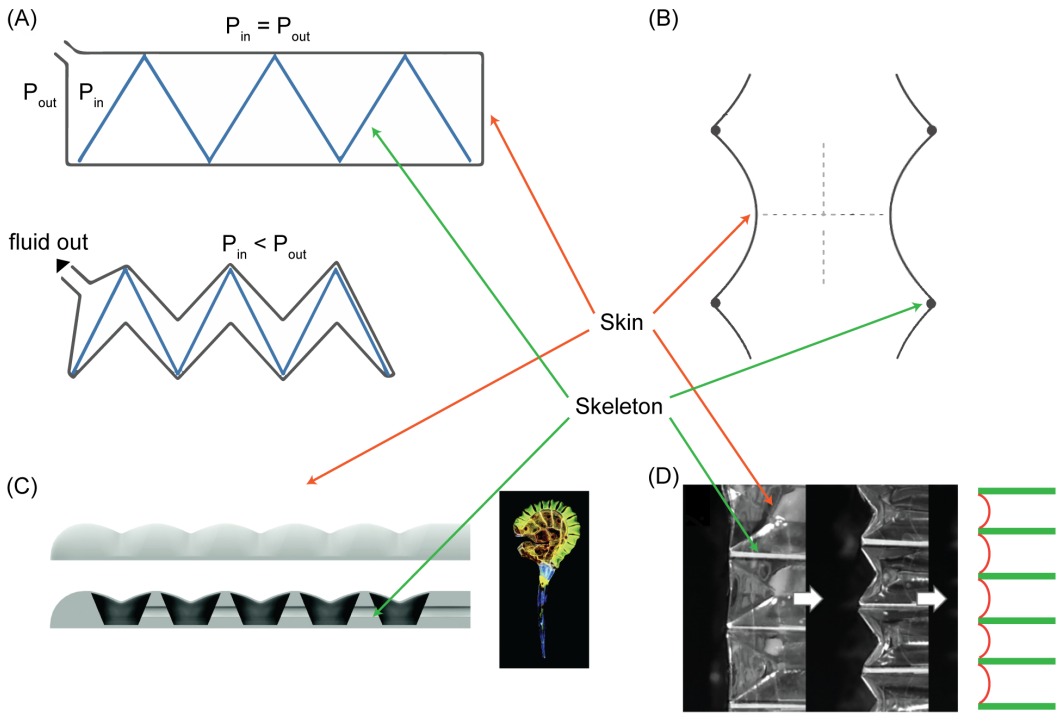

Figure 1-1: Overview of existing skin-skeleton vacuum actuator designs, highlighting the skin and skeleton components. These include (A) FOAMs (Li et al. 2017), (B) Bellows actuators (Felt et al. 2018), (C) bending soft actuators (Tawk et al. 2018), and (D) Origami bellows actuator (Lee et al. 2019). All figure reproductions approved by publishers.[1]

Chapter 2

Formulation of Models

2.1 Theoretical Framework for Geometrical Model

Guided by the virtual work approach described in previous studies [18, 27], we derived a simple generalized formula for the FCP of a vacuum actuator which requires only information on its geometry. As Figure 1-1 illustrates, most soft vacuum actuators with linear contraction motion exhibit volume loss in both the axial (ΔV_a) and radial (ΔV_r) directions. It is beneficial to categorize the volume loss in this way because, while the spatial derivative of the axial volume loss (dV_a/ds) leads to a constant force profile, the derivative of the radial volume loss is responsible for the nonlinearity in the actuator FCP, as will be shown. This also allows for an easy non-dimensional transformation of the output, as can be seen in the brief derivation below, based on the labeled V_r and V_a values from Figure 2-1:

$$V_{T,act} = A_c s - V_r; \qquad V_{T,piston} = A_c s$$

$$\frac{F_{act}}{P} = A_c - \frac{dV_r}{ds}; \qquad \frac{F_{piston}}{P} = A_c$$

$$\frac{F_{act}}{F_{piston}} = F^*_{act} = 1 - \frac{1}{D}\left(\frac{dV_r}{ds}\right) \tag{2.1}$$

where V_T is the total internal volume of the actuator's contractile cell, F is its output force in Newtons, P is the constant actuation pressure and D is a characteristic length

that replaces the cross-sectional area A_c in the case of a 2D simplification of the actuator. The subscripts act and piston refer respectively to the actuator in question and a piston of equivalent cross-sectional area, where a piston is defined as having no radial volume loss (Figure 2-1). F^*_{act} is the piston-scaled force of the actuator, a non-dimensional force or a ratio of the actuator's force output compared to that of its equivalent piston. In this case, the actuator is simplified as a two-dimensional equivalent, so A_c becomes a characteristic radial length, D, while V_r becomes a two-dimensional slice of the lost radial volume. As Equation 2.1 shows, the scaled output force of the actuator is a function of the derivative of the radial volume loss over its contraction s. This assumes a constant pressure and constant bounding cross-sectional area (D). By setting the characteristic length D to 1, Equation 2.1 describes a generalized scale-independent force profile curve.

2.2 Implementation of Geometrical Model

To generalize the concept of radial volume loss, we identify two components that can be used to represent a vacuum actuator in our model: a skin profile and a boundary profile. As Figure 2-2A demonstrates, the model requires that a vacuum actuator be discretized into contractile cells, similar to that used in the derivation. This cell is simplified as a two-dimensional shape with a zero-thickness skin, described by a function f_s, and a set of boundaries, described by the boundary function f_b.

In this work, we focus on modelling the bellows [27] and FOAM [21] actuators, because both fall into the skin-skeleton category, have linear motion, and have been well-described experimentally and analytically in the literature. The bellows actuator has a simple working principle due to the low number of components in its assembly and its minimal skeleton design, while the FOAM actuator is interesting for the resistance of the folded skeleton resistance to contraction, which imparts an opposing spring force to the actuator. In both cases, the characteristic skin function is a parabola of constant length fixed at both ends of the cell, chosen to emulate the profile of the actuator skin as it conforms to the underlying skeleton during contraction.

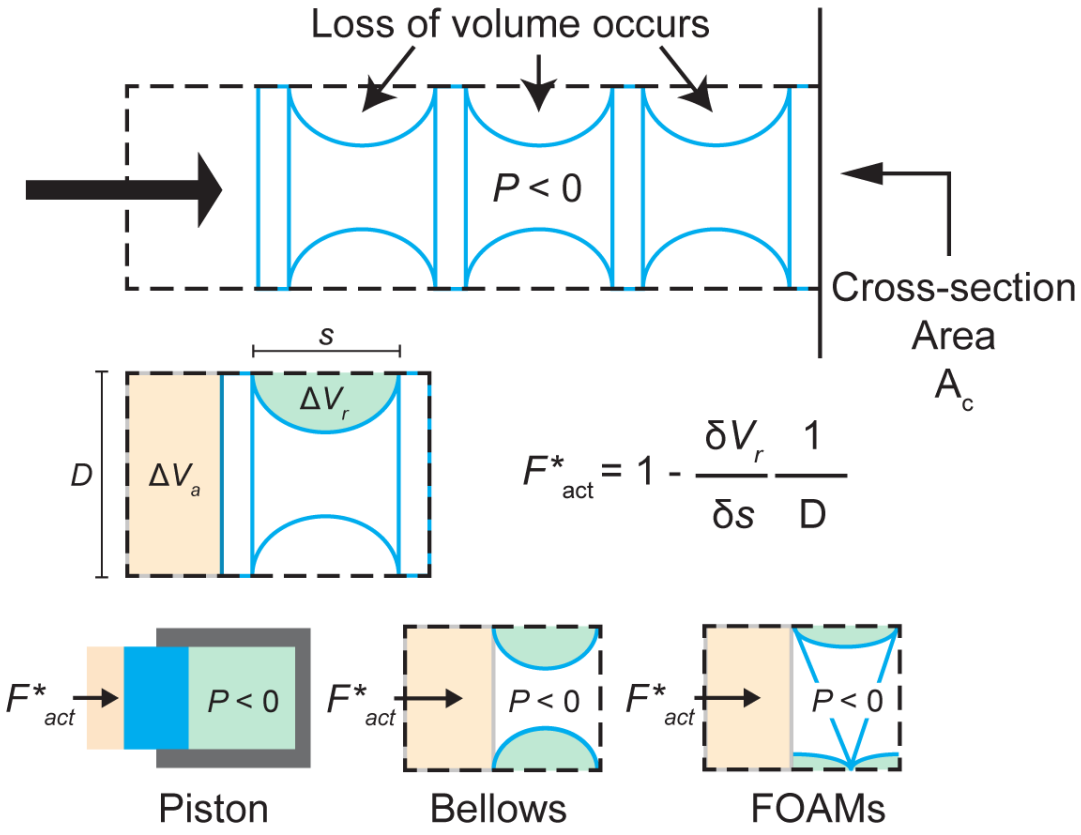

Figure 2-1: A schematic of the general skin-skeleton vacuum actuator working principle, conceptualizing the components for the model derivation, with relevant volume losses labeled. Bottom row shows how Equation (2) can be applied to different actuator designs. ΔV_r = volume loss in radial direction. ΔV_a = volume loss in axial direction. Ac= characteristic radial length. F_act^* = scaled actuator output force. P = actuation pressure. s = current actuator length. D = cross-sectional area.[1]

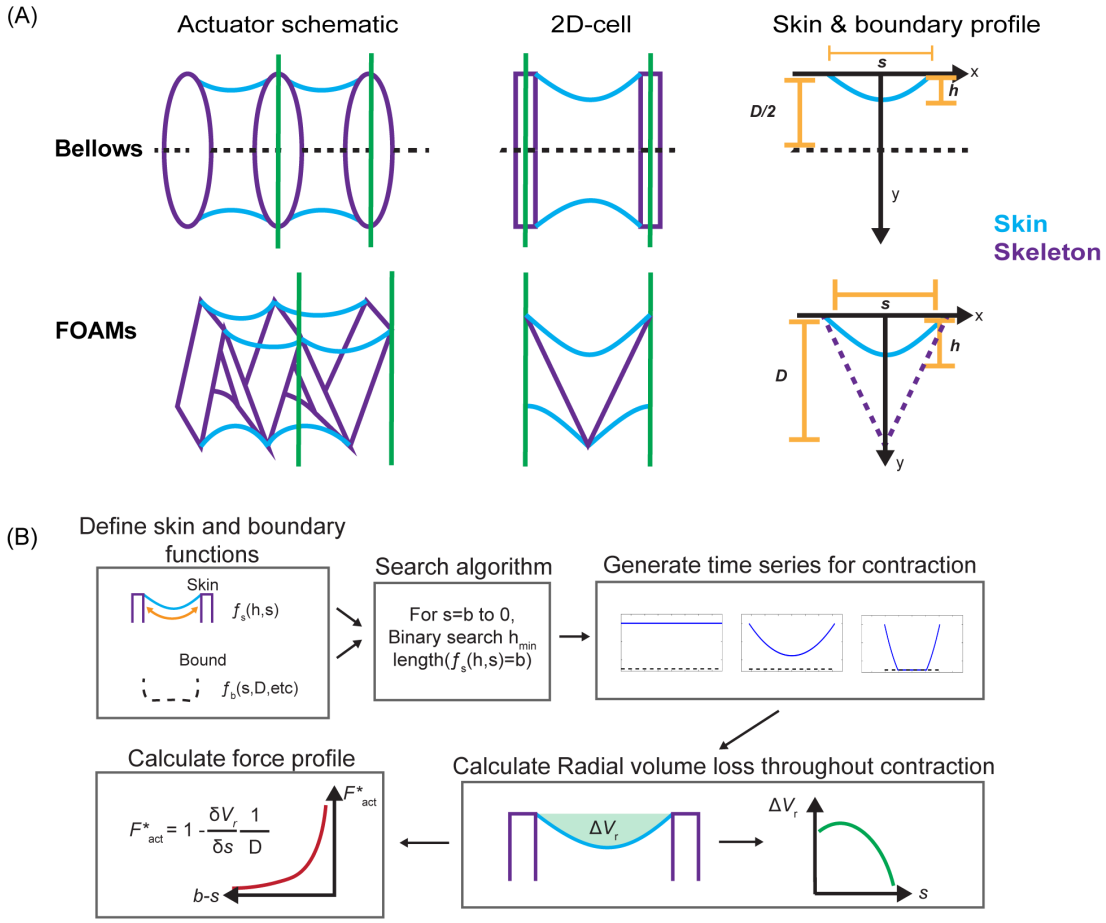

Figure 2-2: (A) Simplifying actuator geometry for virtual work model. (B) A schematic of model implementation. s = length of a contractile cell. h = skin sagging depth. D = actuator cross-sectional area. b = initial spacing between two contractile cells or constant length of skin section. V_r = radial volume loss. F_s = skin function. f_b = boundary function. F_act^* = piston-scaled actuator output force.[1]

$$f_s(s,h)(x) = -h(1 - \frac{x^2}{(s/2)^2}); \qquad -\frac{s}{2} \leq x \leq \frac{s}{2} \tag{2.2}$$

Where s is the length of the contractile cell, h is the skin's "sag depth" into the actuator, and x is the axial coordinate of a point along the skin (Figure 2-2A shows these variables in a schematic). The algorithm can accept alternative skin functions, provided they include the input h for sag depth, as discussed in the model implementation section.

The boundary conditions were defined separately for the bellows and FOAM actuators, as shown in Figure 2-2A. Although there are no defining structural bounds for the bellows actuator skin, a boundary at the midline was defined since the axisymmetry of the actuator causes the skin to contact itself on actuation for cases where the gap distance between rings is greater than one diameter [27]. For the FOAM, the boundary was defined by the zigzag shaped skeleton, which was assumed to have zero thickness. The boundary equations are as follows:

$$f_{b,bellows}(x) = -\frac{D}{2} \tag{2.3}$$

$$f_{b,FOAM}(L,s)(x) = \frac{2d}{s}|x| - d; \qquad d = \sqrt{l_i^2 - \left(\frac{s}{2}\right)^2}; \tag{2.4}$$

where L is the constant length of one of the sections of the zigzag of the FOAM's skeleton, defined as $D \div \cos\left(\frac{\theta_i}{2}\right)$, and d is the height of the skeleton for a given value of s. Figure 2-2A includes a schematic of the skin and boundary functions.

With the specified skin and boundary functions, the FCP can be solved, as illustrated in Figure 2-2B. The major computational section of the model is the process for calculating the geometrical configuration of the skin for each point in the contraction (between contractile cells, equal to the skin length, b, to 0). This is achieved via a binary search algorithm, which attempts to find the lowest value of h that leads to a skin configuration of length b (equal to the initial gap length of b), as the model assumes an inextensible skin. The algorithm requires a function $l_s(h)$, which outputs the length of the skin configuration for a given sag depth h. For a given increment i in the contraction, the binary search starts at $h_{i,1} = h_{i-1,final}$ (or 0 for the first increment), and adds a constant step value to h, updating

the lower bound $h_{i,lower}$ until it reaches a value of h that returns a length greater than the desired target, at which point it sets the upper bound $h_{i,upper}$. The next increment, $h_{i,next}$ is linearly interpolated between $h_{i,lower}$ and $h_{i,upper}$ based on how far from the target section length the from the upper and lower bound configurations are:

$$h_{i,next} = \frac{\left(h_{i,lower} dist_{upper} + h_{i,upper} dist_{lower}\right)}{dist_{upper} + dist_{lower}} \tag{2.5}$$

where $dist_j = |l_s\left(h_{i,j}\right) - b|$. If $h_{i,next}$ is below the target, it becomes $h_{i,lower}$, and similarly for $h_{i,upper}$ in the case that the increment is above the target value. Eventually, this converts to the target value within a tolerance, but to return the smallest valid h value, the function returns only once the upper and lower bounds are close to each other by a certain tolerance. This assumes the section length is monotonically increasing as a function of h, but can be adjusted to account for local maxima/minima using traditional optimization function methods.

The final crucial piece of the algorithm is the skin profile function, which solves the geometrical configuration of the skin for a given h. Given a value for h, it first calculates the skin profile (in this case, always a parabola) and identifies any intercepts with the boundary function. If there is no intercept, it returns the skin profile as a 2D-array of x-y coordinates. If there is an intercept with the boundary, the function draws the section of the parabola up to the intercept, then draws the section of the boundary for the remainder of the way or until the second intercept. The process is repeated recursively to complete a profile.

The result of the binary search function and the skin profile function working in unison is a skin configuration for each contraction increment i, from ¬s at full to zero length, referred to as the "time series" in Figure 2-2B. This represents the shape of the actuator's skin throughout the contraction. If, at some increment, the skin profile can no longer be solved, as is the case for the bellows actuators once the skin is in full contact with the boundary, that increment defines the end of the contraction. The V_r value for each increment is calculated and then numerically differentiated following the function for F^*_{act} to finally generate the FCP.

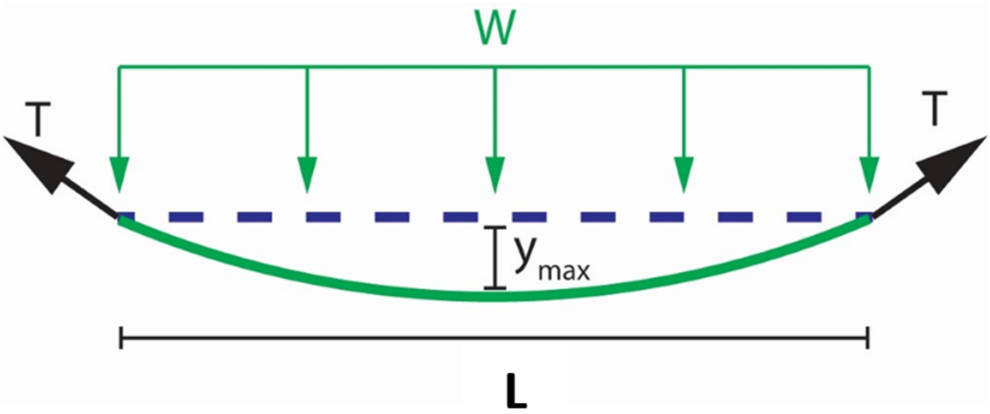

Figure 2-3: Schematic of cable under uniform load for Roark's formula. Used as a parallel to the actuator's skin under vacuum loading.[1]

2.3 Finite Element Modelling (FEM) to Supplement Theory – Scaling Factor

2.3.1 Scaling Factor Theoretical Basis

From the theoretical derivation of the model above, one can see that it assumes an inextensible skin, and is reliant only on the geometry of the skin and boundary function, as well as an aspect ratio of radial to axial dimensions. In the physical case, the inextensible skin extension does not fully apply, as the skin experiences some strain, which would translate into work that is not used for force production. It follows logically that the physical properties of the skin have an effect on the magnitude of the force output. To address this, we developed a scaling factor (between 0 and 1) to be applied to the output of the model, based on Roark's formula [34], which describes the strain of a cable in tension with a distributed load – as that resembles closely the state of the skin at the initial zero-contraction configuration of the actuator.

The schematic in Figure 2-3 shows the layout for Roark's formula applied to a flexible cable, as described in [34]), here used to describe the skin, where y_{max} is the skin's sagging

depth, T is the tension on the skin equivalent to the output force, w is a distributed load in N/m equivalent to the internal pressure, E is the skin material's Young's Modulus, and A is the cross-sectional area of the skin (not of the actuator), and, L is the gap between rings. The equation is applied to the maximum force output of the actuators as it is valid for small deflections, y_{max}, of a cable with no initial sag, which in our FEM models corresponds to the initial zero-contraction point.

By plugging in the equation for y_{max} into the equation for T, one finds the following:

$$T = \frac{(64EA)^{1/3}(wL)^{2/3}}{8 * 3^{1/3}} \tag{2.6}$$

Assuming the cross-sectional area of the skin to be $A = t * P_{act}$, where t is the skin thickness and P_{act} is the perimeter of the actuator's cross section, we find that

$$T \sim (E * t)^{1/3} \tag{2.7}$$

Note there are other terms in the expression for T, but they are all incorporated in our model either as geometrical parameters or in the non-dimensional piston-scaled force, so we neglect them from the relationship for the scaling factor. The purpose of the scaling factor is to accommodate for aspects of the construction of an actuator that were not addressed by the virtual work model, namely the thickness and stiffness of the skin, which are known to be relevant and application-specific. As Roark's formula for a cable shows, E and t are the only missing application-specific components that are not incorporated in the model.

2.3.2 FEM of Bellows Actuators

To confirm the derivation of Equation 2.7 and the relationship between output force and Young's Modulus and skin thickness, and to derive of an informed function for the scaling factor to be applied to the virtual work model, we developed an explicit FEM model of a bellows actuator Abaqus/Explicit (Dassault Systèmes). This model was used to easily vary combinations of skin properties to extract trends from the comparison between the virtual work model-predicted output and that of the FEM. Figure 2-4 depicts the FEM setup. S4R shell elements were used to model the skin, and a linear elastic material property was

applied with varying Young's Moduli in the range of 10-500MPa with a Poisson's ratio of 0.3. The skin section thickness was varied from 0.02 to 0.35mm. To simulate the rings, radial displacement constraints were applied to node pairs around the skin at desired gaps, restricting the motion of these selected nodes to be strictly along the actuator's long axis. Finally, a general frictionless self-contacting constraint was applied to the skin shell. The system was given a total of three rings (two contractile cells). A rectangular prism shape (square cross-section of 20x20mm) was used for the actuator, as it allowed more consistent meshing and faster solution times than a circular cross section actuator – both circular and square shapes were compared, and output force profiles were showed the same outputs given the same cross-sectional area.

A fixed condition was applied to the nodes at one end face of the skin, and a variable displacement condition was applied to the nodes at the other end. The model was run with the following actuation steps, called the load test procedure. First, a vacuum pressure of -5 kPa (decreasing linearly from zero over 0.5 simulation time units) was applied inside the skin while the two ends of the actuator were held fixed. Once the pressure reached the desired preload, the pressure was held constant and a constant-velocity displacement boundary condition was applied to one end of the skin, while the other was kept fixed, allowing the actuator to contract. The magnitude of the displacement was chosen to match $7/8^{ths}$ (87.5%) of the contractile length of the actuator – in the case of the 20x20mm, R=1 actuator, the contractile length for two cells is 40mm, so a displacement of 35mm was applied. The axial reaction force at the fixed end of the skin was then extracted to quantify the FCP of the actuator.

2.3.3 Fitting of Scaling Factor Equation from FEM Experiments

After performing the multiple FEM experiments, varying the Young's Modulus and thickness of the actuator skin, we were able to confirm that the two parameters had effects on the output force magnitude predicted by Roark's formula. Figure 2-5 shows the results of the FEM for varying stiffnesses (A) and thickness (B), as well as the trends in the maximum output forces for varying stiffness (C) and thickness (D). Finally Figure 2-5E shows the

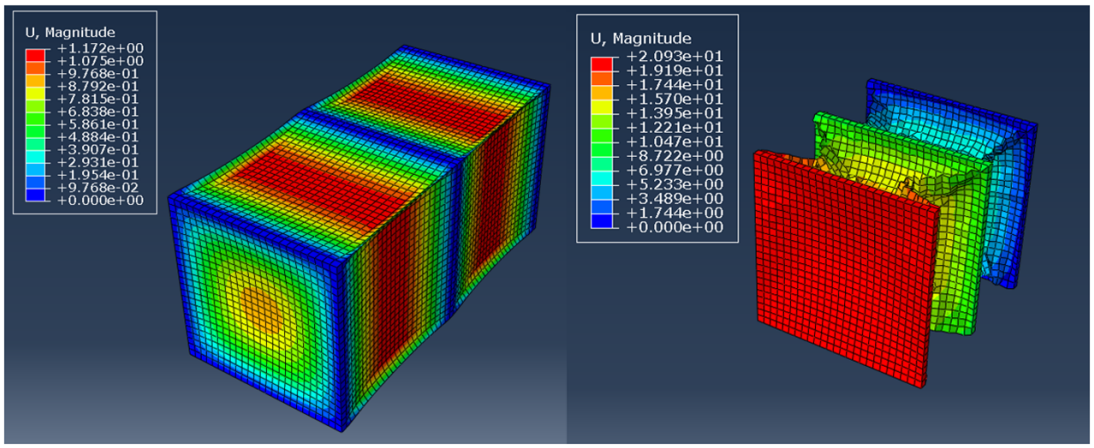

Figure 2-4: Results FEM setup for extracting FCP of a bellows actuator. In this case, actuator cross-section is 20x20mm and R = 1. Showing zero and 50% contraction. E = 237 MPa and t = 0.1 mm. Displacement, U, in mm.[1]

direct relationship between maximum output force and the cubed root of $E*t$.

To derive the function for a scaling factor based on the material properties, we first extracted the FCP from the FEM models and scaled the output force by the force of an equivalent piston, such that it could be compared with the output from the virtual work model ($F_{piston} = P*Ac = 2N$, where P is the actuation pressure and Ac is the cross-sectional area of the actuator's shape, or width times height in the rectangular case). We then divided the maximum scaled force for each FEM experiment with the maximum force predicted by our virtual work model, to find the scaling factor necessary to match the force magnitudes between the two models for each E-t pairing. After finding that the trend between $(E*t)^{1/3}$ and the scaling factor was linear as in Figure 2-5(E), we applied a linear fit to the FEM data to solve for our scaling factor equation:

$$s = 0.1992*(Et)^{1/3} + 0.0067 \tag{2.8}$$

where s is the scaling factor to be multiplied with the virtual work model to estimate the force output for given skin properties.

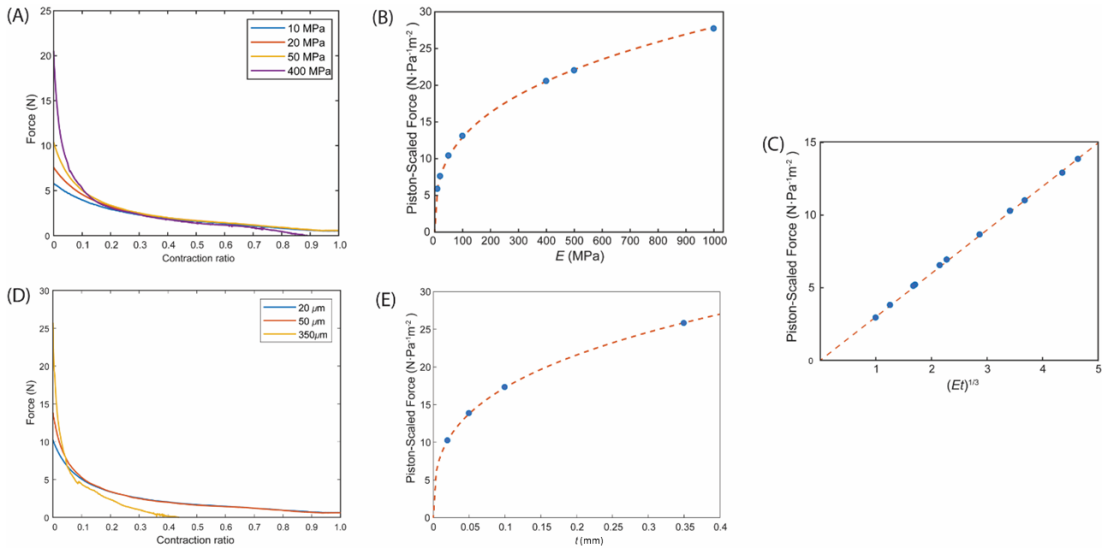

Figure 2-5: Analysis of actuator skin material-dependent scaling factor. (A) and (D) show the FCPs for varying skin stiffnesses and thicknesses respectively (for a two-cell 20x20mm cross sectional area bellows actuator of R = 1). (B) and (E) show the piston-scaled maximum force output from the FCPs for varying stiffnesses and thicknesses respectively. (C) is the joint trend for maximum scaled force and $(Et)^{1/3}$, where the cubed root relation is extracted from Roark's Formula and is used to quantify the skin's tensile stiffness, where E is Young's modulus (MPa) and t is the thickness (mm) of the skin material used in the actuator.[1]

2.4 FEM to Supplement Theory – Restoring Force Loss

2.4.1 FEM of FOAM Actuators

In the case that an actuator has a non-negligible internal restoring spring force that resists its contraction – such as the case of the FOAM with its zig-zag skeleton – we hypothesized that one can super-impose the calculated spring resistance force with the virtual work model FCP to reach an accurate estimate of the actuator's true FCP.

To estimate the spring resistance force from skeleton, a quasi-static FEM model of a FOAM skeleton was created in Abaqus/Explicit. The skeleton was modeled with a 30-degree fold angle, 50 x 20 x 10mm bounding dimensions, and 1mm thickness and modelled as a linearly elastic polyvinyl chloride plastic (Density = 1.4 g/cc, Young's Modulus = 2.4GPa, Poisson's Ratio = 0.3 as defined by the manufacturer specifications) and 8-node linear brick, reduced integration, hourglass control (C3D8R) elements. This skeleton was fixed at one end, restricting both rotation and displacement, and a displacement boundary condition of 35 mm was applied to the other end, compressing the skeleton gradually over time. The reaction force of the skeleton in the axial direction was extracted to quantify its spring resistance.

In parallel, a full FOAM model was generated, where the same skeleton was surrounded by a bounding skin. The skin was modelled using a thermoplastic elastomer with high stiffness (Density = 0.8 g/cc, Young's Modulus = 600 MPa, Poisson's ratio = 0.3, average properties from MatWeb) with 4-node, quadrilateral, stress/displacement shell elements (S4R) of thickness 0.02 mm, with a membrane idealization (such that the skin is dominated by tensile forces). The same load test procedure used for extracting the FCP of the bellows actuator was used for the FOAM model, except the pressure applied was -70kPa and the contraction displacement was equal to 25mm. A general, frictionless contact interaction was defined for all elements in the simulation. For the analysis, we compared the FCP generated by the FOAM actuator in the FEM and the net force predicted by the virtual work model, which was calculated as the pure FCP from the geometrical virtual work model subtracted by the skeleton spring force obtained in the FEM. The results of this comparison are included in the next chapter.

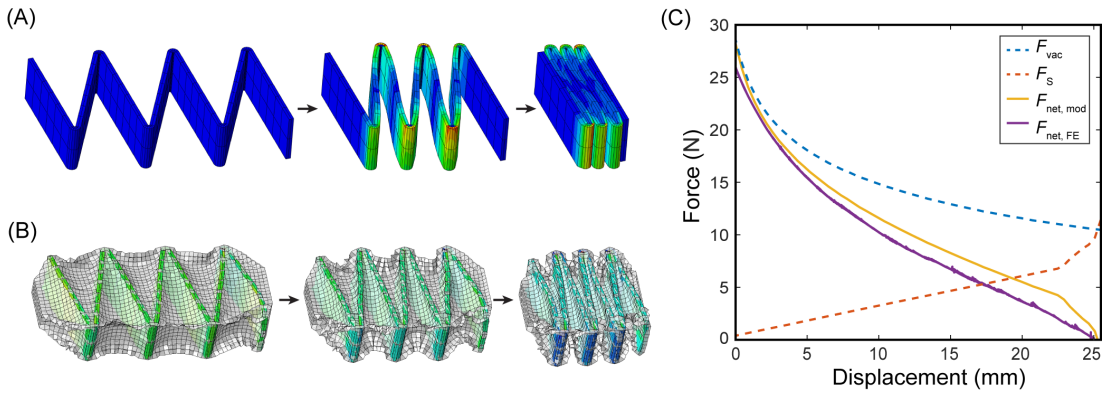

Figure 2-6: (A) Deformation of a 30-deg skeleton during compression test in a Finite Element (FE) model. (B) Free contraction of FOAM actuator containing the same skeleton under constant negative pressure in a FE setup. (C) A comparison of FE Model and virtual work model for FOAM actuators for $\theta = 30^o$, P = -70kPa. F_s = Skeleton spring force predicted by FE. F_{vac} = Force predicted by virtual work model without spring force.$F_{net,mod} = F_{vac} - F_s$ = Net force predicted by the MATLAB model. $F_{net,FE}$ = FOAM force predicted by FE.[1]

2.4.2 Results from Finite Element Modelling of FOAM Actuators

Figure 2-6A shows deformation of skeleton during spring compression test performed in FEM, and Figure 2-6B shows contraction of a FOAM actuator using the same skeleton under constant pressure. Figure 2-6C compares the FCPs generated with the FEM ($F_{net,FE}$) and virtual work models ($F_{net,mod}$), demonstrating that the virtual work model can accurately describe a force profile when the skeleton spring reaction force is accounted for by subtracting it from the model predicted force. The peak force from the virtual work model was within a 7% error and the full contraction length was within a 1% error.

Chapter 3

Model Characterization and Validation

3.1 Model Parametric Characterization

3.1.1 Force Contraction Profile Explanation

Figure 3-1 illustrates the shape of a force-contraction profile for a bellows actuator, overlaid with a simplified time series of the skin profiles generated by the model. As shown, the large force output at the start of the contraction is directly tied to the large relative change in radial volume at the beginning, as the skin experiences the greatest drop. In later stages, the output force curve flattens as the skin gets closer to its final configuration and the loss in radial volume decreases.

3.1.2 Parameter Sweep

We performed a parametric sweep of different ring gap-diameter ratios using our virtual work model to evaluate the effect of the ring spacing on the force profile of bellows actuators. Figure 3-2A shows the calculated force profiles for varying ring gap-diameter ratios, $R = b/D$. The peak force decreases with decreasing gap distance, the force profile becomes more linear with decreasing gap distance, and gap distances greater than one diameter in length lead to a maximum scaled contraction equal to R^{-1}. Figure 3-2B overlays the full parameter sweep of values of R from 0 to 4, demonstrating how much stroke and force can be generated by an ideal vacuum bellows actuator for the given ring and gap dimensions.

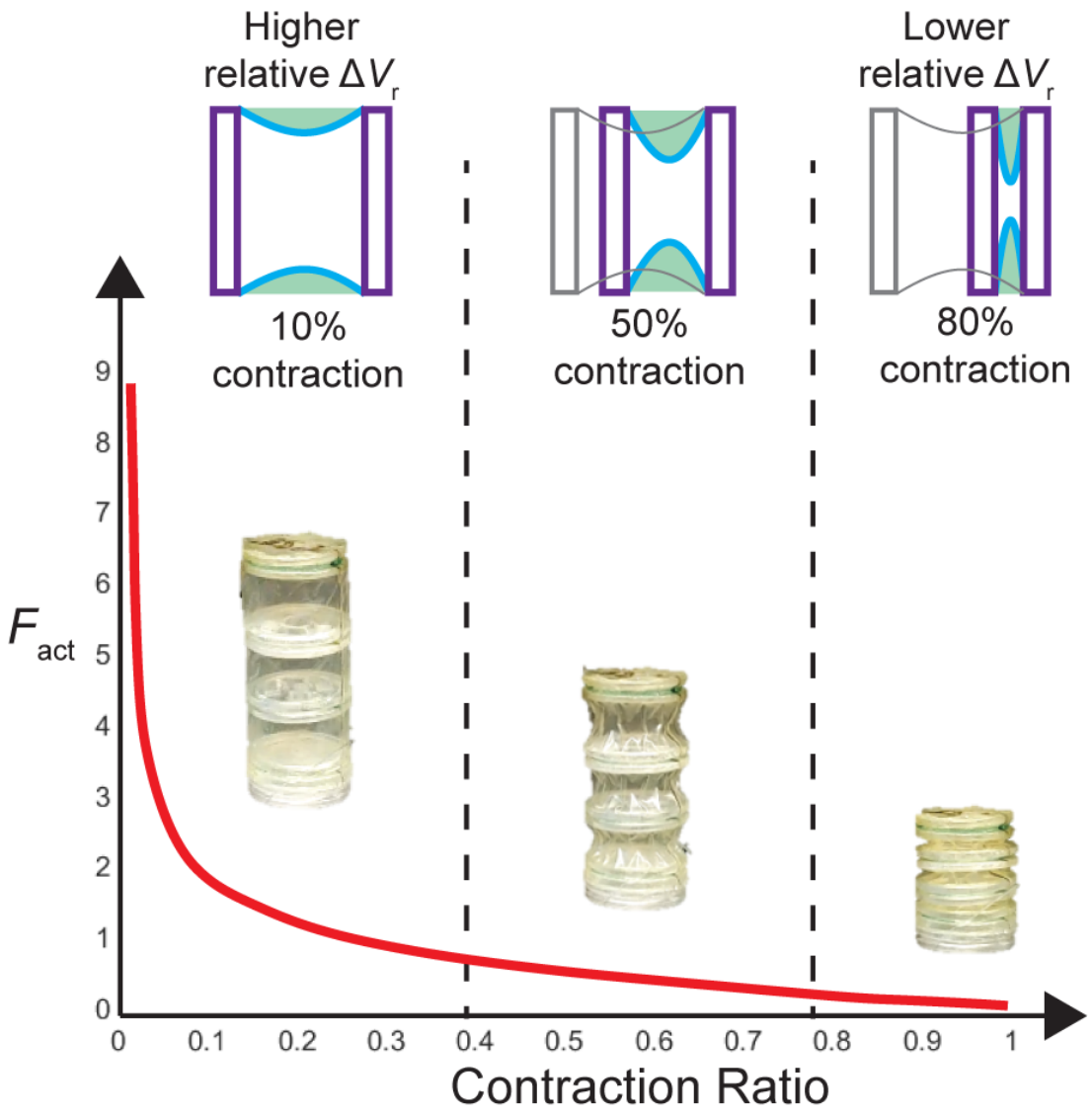

Figure 3-1: Illustration of the force-contraction profile of bellows actuators, depicting the geometrical reasoning around the shape of the profile based on the concept of the virtual work function. Initially, the actuator skin is completely straight, and as it contracts, the parabolic profile leads to a rapid loss in radial volume, which justifies the large initial force value (large derivative). As the contraction nears its middle and end, the parabolic skin profile sags less and becomes narrower, leading to a smaller rate of volume loss and thus a smaller piston-scaled force.[1]

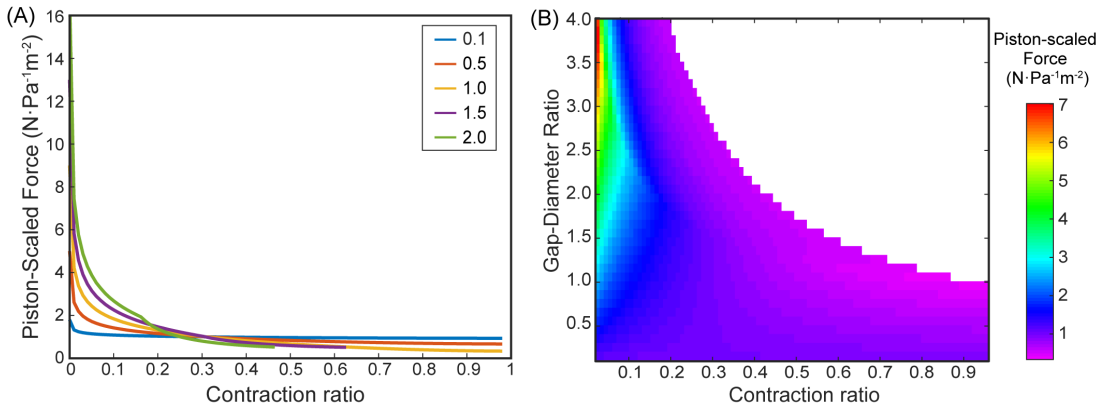

Figure 3-2: Virtual work model for vacuum bellows actuator with varying ring distances. (A) Force-contraction profile for varying gap-diameter ratios (R) = 0.1, 0.5, 1, 1.5, 2, showing the trends caused by varying ring gap. (B) A heat map from a high-resolution parameter sweep of the gap-diameter ratio. The color bar indicates piston-scaled force predicted by the model, and the contraction ratio is cut off at 0.04 for the purposes of visualizing the contrast throughout the heat map (large magnitudes past 0.04 lead to colors focused on high values).[1]

First, we predict the FCP of the FOAMs geometry without an additional spring factor, only considering the effect of its triangular bounding function shape. The skeleton angle θ in FOAM actuators is analogous to the ring gap distance R in bellows actuators, as the fold-to-fold distance in the zigzag skeleton is a function of θ: $R = 2\tan\left(\frac{\theta}{2}\right)$. Figure 3-3 demonstrates the FCPs predicted from the FOAM boundary setup for varying θ in the absence of spring force.

3.1.3 Varying Skin Profile Shape for Bellows Actuators

To explore the relevance of different skin profile functions, we performed a simple modelling run, where three different conic sections were used as the skin profile for a bellows actuator of R = 1: a parabola (as implemented in the main body of this thesis), a hyperbola, and a half-ellipse with its vertices at the interface with the rings. The force-contraction profile for each was calculated and they are compared in Figure A-1. Generally, there were no major differences between different profiles, though the parabola and hyperbola FCP follow each other virtually identically, while the ellipse FCP experiences a slightly flatter profile. This is likely because the ellipse experiences a more gradual drop in sag depth

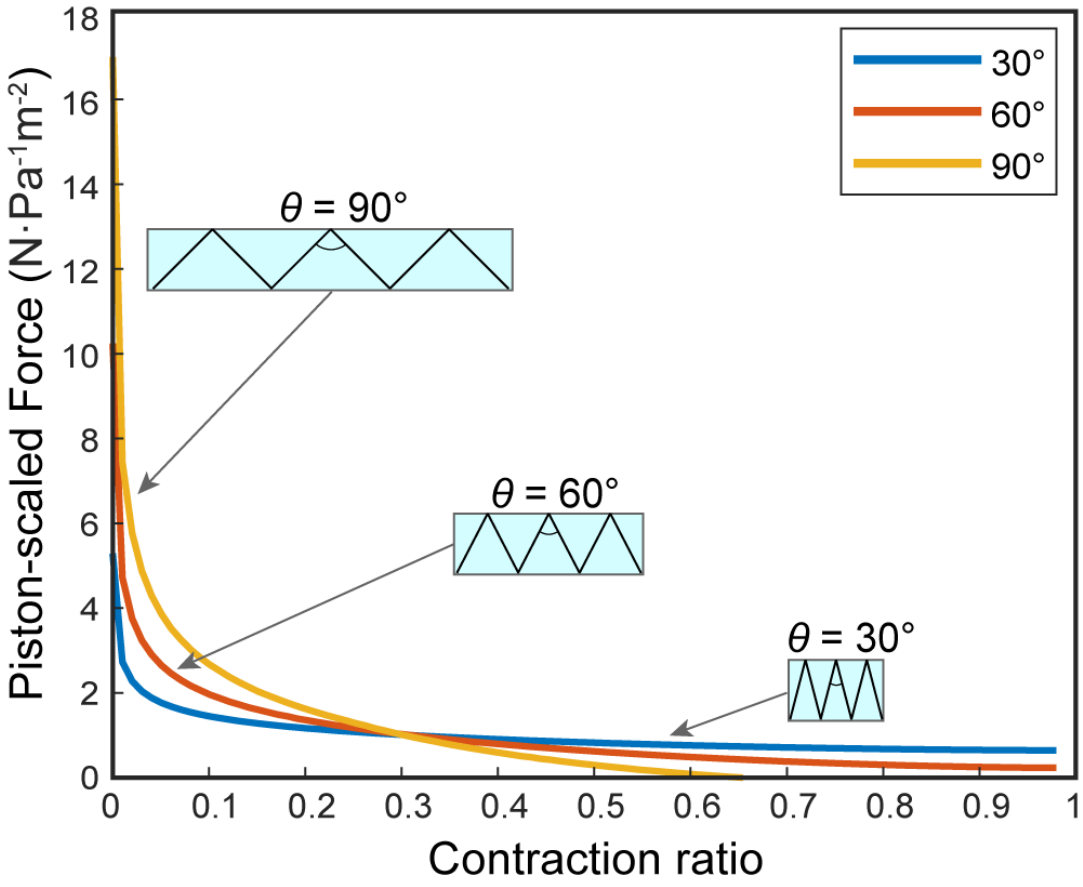

Figure 3-3: The virtual work model prediction of force-contraction profile for FOAM actuators with skeleton angles (θ) = 30, 60, and 90 degrees. The profiles are based only on the geometrical features, without the inclusion of spring force.[1]

during contraction, whereas the hyperbola and parabola both lower more quickly. Overall, this shows the different conical sections similarly approximate a simple skin profile. Other more complex functions, such as the volume minimizing skin profile function in Felt et al. 2017[27], may lead to a more noticeable difference, despite following the same trend. More complex skin geometries, such as for an origami-based actuator, would require more complex skin profile functions with more variable rule-based shapes.

3.2 Methods

3.2.1 Fabrication of Bellows Actuators

A vacuum bellows actuator consists of a thin tubular membrane surrounding rigid rings that are evenly spaced along the axis of the tube. Two 0.04 mm polyethylene sheets (McMaster-Carr, 7889T28) were sealed along two edges at a nominal width of 40mm for 4 s using an impulse sealer (Hacona, H-6705) to make a 25mm-diameter tubular membrane. For the rigid rings, a three-part assembly consisting of one concentric ring surrounded by two thinner annular rings placed at the edges of the inner ring was fabricated. The inner ring was made of 4.76 mm acrylic (McMaster-Carr) and laser cut to form an outer diameter of 40 mm with minor cut features that enable airflow between segments for middle segments and a 3.175 mm center hole for placing the tubing at one end. The outer annular rings were made from 1.59 mm acrylic with an inner diameter of 20 mm and outer diameter of 25 mm, and were bonded to the inner ring using cyanoacrylate (Loctite). The assembled rigid rings were positioned inside the membrane and orthogonally to the wall, and then secured around the groove created in the ring assembly using fishing line (9442T2, McMaster-Carr). The remainder of the ring assemblies were positioned along the membrane at the desired spacing and fastened in similar way. A 3.175 mm outer-diameter polyurethane tube was inserted through the first ring assembly for vacuum supply and the ends of the membrane were sealed to the acrylic using cyanoacrylate adhesive and SilPoxy (Smooth-On). An image of the bellows actuator is shown in Figure 3-4B.

3.2.2 Fabrication of FOAM Actuators

FOAM actuators consist of a thin skin layer surrounding a rigid zigzag structure that serves as the skeleton. For the skin layer, we sealed two sheets of 0.05 mm-thick thermoplastic elastomer (Fibreglast) using an impulse sealer for 20 s along two edges at a nominal spacing of 53 mm. For the skeleton, 0.254 mm-thick polyester sheet (McMaster-Carr) was laser cut in a series of 10 segments (L = 20 mm, W = 40 mm) with minor features on each segment to allow air flow and perforated lines between the segments to help folding. The skeleton was manually folded along the perforated lines at desired angles of 30, 60, and 90 degrees. For assembly, the skeleton was inserted into the skin membrane and sealed using an impulse sealer at skeleton lengths of 60, 110, and 150 mm, respectively. A piece of PTFE was used to create a gap in the seal for subsequent tube insertion. To ensure that the skeleton material did not slide inside the skin during actuation, we used thermoformable anchors at the ends of the skeleton that were sealed with the skin, and therefore fixed at each end. An image of the FOAM actuator is shown in Figure 3-4A.

3.2.3 Experimental Methods

Force Contraction Profile Experiments

To obtain FCPs for each actuator, we measured the force-displacement curve using a mechanical tensile tester (Instron 5944) for all actuators. The actuators were held at the ends with a 2-kN load cell (Figure 3-5) and allowed to contract at a rate of 100 mm/min until the force reached zero. Each actuator's length was measured to account for variability in manufacturing and to allow for a more accurate scaling of the percent contraction when analyzing data. Constant vacuum pressures of -15 kPa for the vacuum bellows and -25 kPa for the FOAM actuators were applied throughout the test using a manual vacuum gauge (IRV10-N07, SMC). Actuators were held at full extended length when vacuum was first applied before beginning the experiment to allow the actuator to begin at full vacuum, where full length is defined by clamping the actuator on the tensile tester and displacing the clamps until the point the actuator begins to be in tension . Actuation pressure was measured throughout the experiment using a TruWave pressure sensor (Edwards Lifesciences)

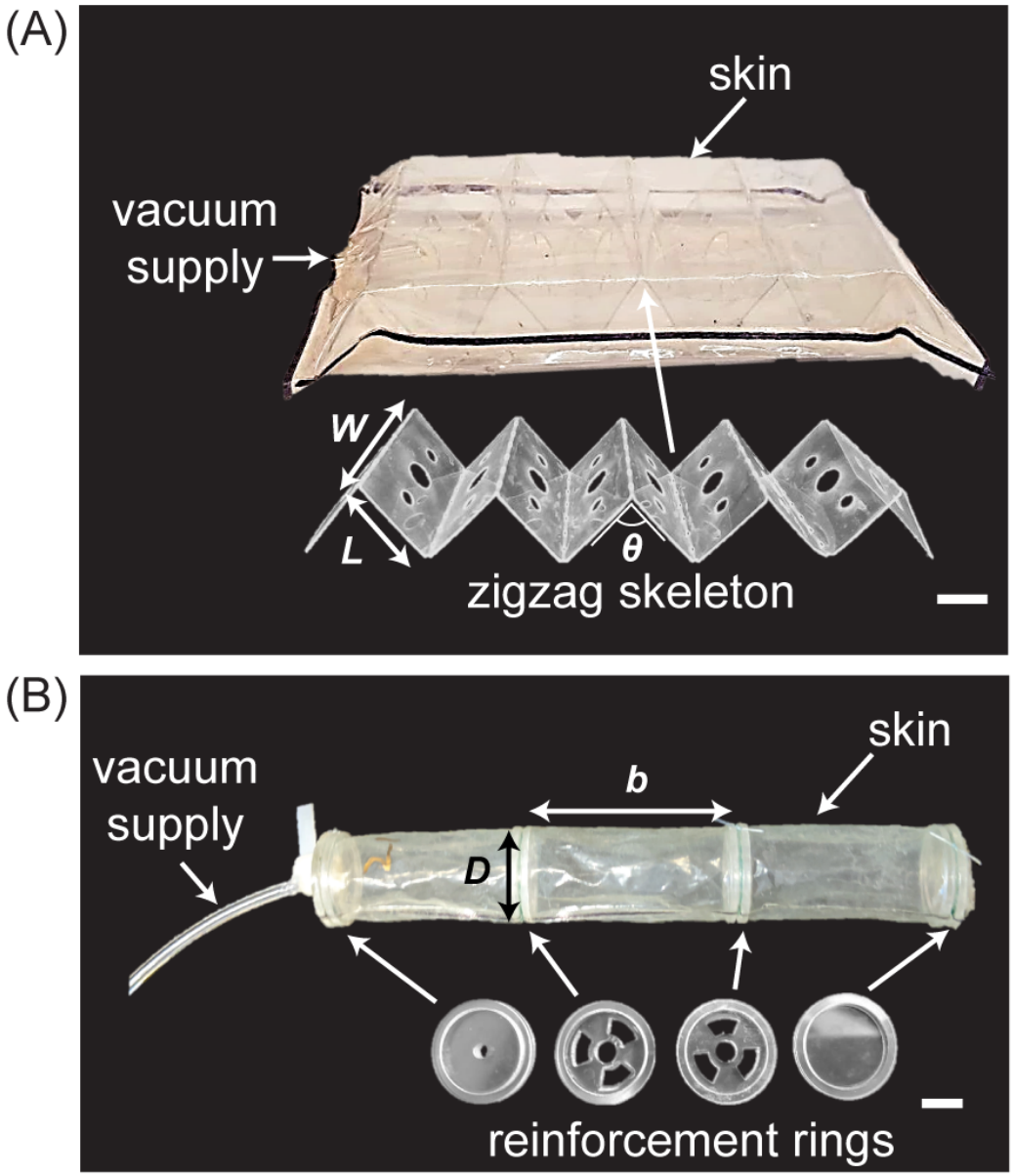

Figure 3-4: Experimental setup for measuring the FCP of bellows (left) and FOAMs (right) actuators. Vacuum was applied through tubes at bottom of images, past a manual pressure regulator.[1]

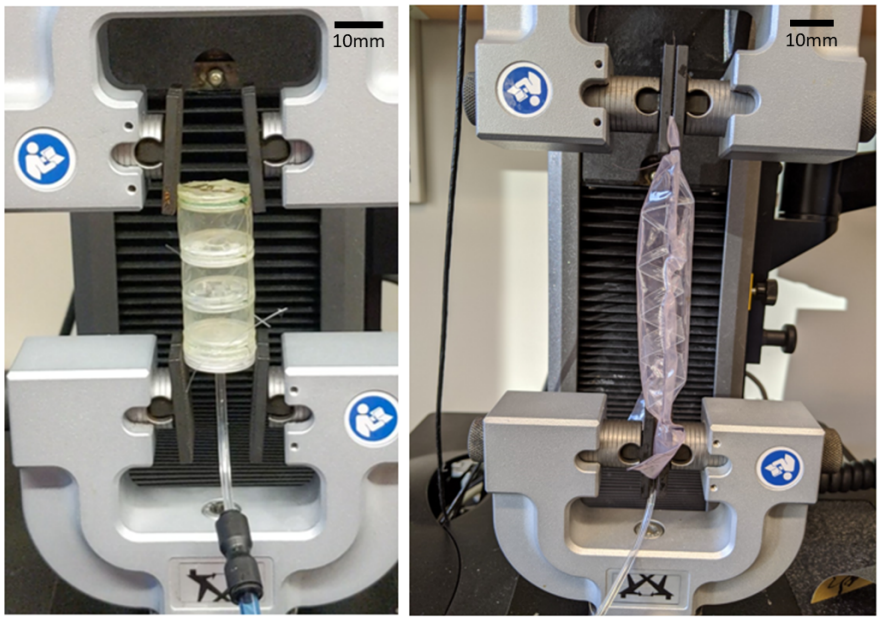

Figure 3-5: Experimental setup for measuring the FCP of bellows (left) and FOAMs (right) actuators. Vacuum was applied through tubes at bottom of images, past a manual pressure regulator.[1]

and was found to hover around an average value – the average pressure for each actuator was used for normalizing the measured output forces. For both Bellows and FOAM actuators, three replicates (n=3) were used for each experiment (i.e. n=3 for each value of R for bellows, and each value of θ for FOAMs).

Skin Material Tensile Testing

To compare the mechanical properties of different skin materials, a uniaxial tensile test was performed on an Instron 5944 at a rate of 1 mm/min. All rectangular test specimens had widths of 20 mm and lengths of 40 mm. The thickness of the skin materials was 0.04 mm for the polyethylene film and 0.05 mm for the thermoplastic elastomer. The corresponding Young's modulus was obtained by taking the best fit slope between strains of 0% to 5%, and the average value (n = 5) was used for scaling the forces in the model based on the scaling factor equation in Chapter 2.

Compression Testing of FOAM Skeleton

To characterize the spring force generated by the skeletons in FOAM actuators, we measured the force exerted by 30-degree zigzag skeletons during compressive loading at a rate of 100 mm/min on a mechanical tensile tester (Instron 5944). The spring constant was derived by taking the slope of the force-displacement graphs and the mean value (n = 3) was used to model the spring force for the FOAM actuators. Figure A-2 shows the experimental data from compressing the three skeletons.

3.3 Experimental Results

3.3.1 Force Contraction Profile Experiments – Bellows Actuators

To validate the model experimentally, we measured the force-contraction behavior of bellows actuators with varying gap ratios, R, of 0.5, 1, and 2. Figure 3-6 shows the piston-scaled force produced by the actuator over the scaled contraction (defined as displacement divided by the actuator length). As a comparison, the virtual work model FCP with the equivalent R is overlaid with the results, after a magnitude scaling factor is applied. This factor accounts for the material properties of the actuator skin, which has some extensibility compared to the inextensible skin assumption in the model. We derived a relationship for the scaling factor through a set of FEM experiments extracting the FCP of a bellows actuator with varying skin thicknesses and stiffnesses, from which we could derive an empirical relationship between output force and Young's modulus (E) and skin thickness (t) (See Figure 2-5). We found the scaling factor is a function of $(Et)^{1/3}$, which agrees with Roark's formula for the tension in a cable with a distributed load [34] – see Supplementary Material section 1.1 for further details. Li et al. (2017)[21] observed the relevance of skin Young's modulus and thickness for the output of vacuum actuators, which informed our decision to develop this scaling factor. For our bellows actuators, which use a 0.04 mm thick polyethylene film as the skin material (E = 127MPa), we scaled the output force predicted by our model by 0.35, calculated through our derived scaling factor equation (see Equation 2.8).

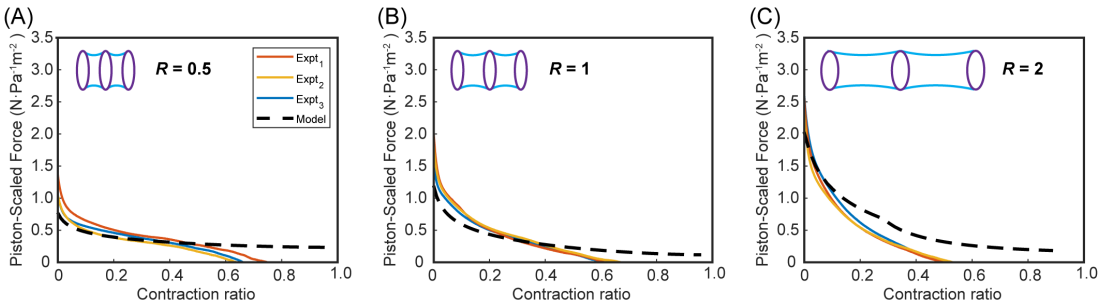

Figure 3-6: The force-contraction profile for vacuum bellows actuators in the experimental and scaled virtual work model for varying ring gap-diameter ratios (A) R = 0.5, (B) R = 1, (C) R=2 for a ring diameter of 25 mm. Number of experiments, n = 3.[1]

3.3.2 Force Contraction Profile Experiments – FOAM Actuators

Figure 3-7 shows the normalized force-contraction curves for three samples each of FOAM actuators with varying skeleton angles of θ = 30, 60, 90 degrees. As expected, higher-degree FOAMs display higher forces compared to lower degree FOAM actuators while displaying lower contraction, which is consistent to the angle-varying trend in Figure 3-3. The predicted force from the virtual work model after using a skin material scaling factor of 0.5 (calculated from scaling factor trend for thickness of 0.05mm and Young's Modulus of 309MPa, using Equation 2.8) is also shown in Figure 3-7. The spring constant was measured from the skeletons as described previously, and the average value of 46.2N/mm (Figure A-2) was used as a linear spring approximation for all three models. After subtracting the corresponding spring force, the net force predicted by the virtual work closely matches the experimental force profile and allows to predict the maximum contraction much more closely as shown in Figure 3-7.

3.3.3 Compression Testing for Bellows Skin Restoring Force

We hypothesize that one of the reasons for the discrepancy between our model and the experimental results for the bellows actuators is that the actuator's skin imparts a restoring force especially towards the end of the contraction, where our model diverges most from the experiment. To test this hypothesis and quantify the significance of the bellows actuator's restoring force, we performed an experiment on the set of four bellows actuators with an R

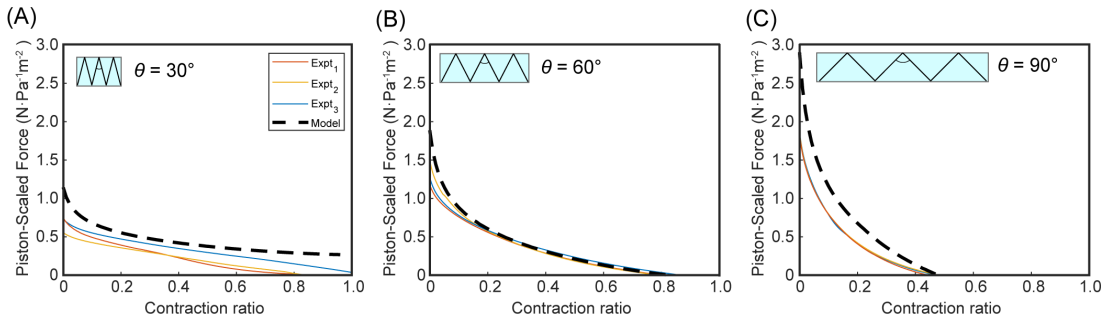

Figure 3-7: Force-contraction profile for FOAM actuators in experimental and virtual work model for varying skeleton angles [θ] ;(A) 30^o, (B) 60^o, (C) 90^o. Model = predicted net force = (pressure-only force without skeleton) - (skeleton spring force). Number of experiments, n = 3.[1]

of 1 used for the results in Figure 3-6.

One contractile cell of the actuator was held on a mechanical tensile tester (Instron 5944) by clamping two adjacent rings. The cell was held at a slight tension, a vacuum of -15kPa was applied, and cell was compressed at 60mm/min, until the output force was equal to zero. The displacement at this point (end of contraction) was recorded. The actuator's contractile cell was brought back to its original tensile position, the vacuum was turned off and the compression was repeated until a force greater than 5N was reached (signaling the rings of the cell were in contact). The force-displacement curve for this compression is the actuator's nonlinear restoring force, and it was recorded. The data from the restoring force was then subtracted from the FCP for a bellows actuator of $R = 1$ calculated by the virtual work model and the model's zero-force point was compared with the experimentally recorded zero-force point for each of the four measured actuators.

Figure A-3 shows the results for the four separately tested actuators, given the varying contraction distances (zero-force points) and restoring force curves. The model-estimated end-contraction points (where the plot crosses zero force) were extracted and compared with the measured end-contraction points, with an average error of 14%. This shows a significant improvement in the model's ability to estimate the FCP of these actuators and supports the hypothesis that neglecting the loss due to the skin's restoring force was a source of disagreement between our idealized model and the experimental measurements in Figure 3-2.

Chapter 4

Limb Flexion Case Study Application of a Model

4.1 Introduction and Case Study Setup

One often explored use of soft robotic actuation is in the field of exoskeletons [8, 9], where the actuated systems are typically in contact with humans and driving human motion. Based on this existing work, we formulated a hypothetical case study to demonstrate the utility of the vacuum actuator FCP models in designing a physiotherapeutic exoskeleton.

Spina Bifida is a birth defect of the spine that affects 1,400 newborn children per year in the US alone [35], and may lead to motor deficiencies, including leg mobility, especially in its most severe form – Spina Bifida Mylomeningocele – which requires early postnatal surgery and is associated with a variety of other neuromuscular irregularities [35]. To address the leg mobility issues, there are a variety of physiotherapeutic approaches, including passive mobility exercises to preserve joint range of motion while the child develops more control and mobility of their legs [36, 37]. Passive range of motion exercises involve the manual motion of a child's joint by another individual (caretaker or healthcare professional), and in the case of Spina Bifida patients, is to be repeated 2-3 times a day, and the number of times and length for each exercise may be increased in cases that are more severe [36, 37].

Inspired by the need for passive leg flexion exercises in infants to mitigate the negative

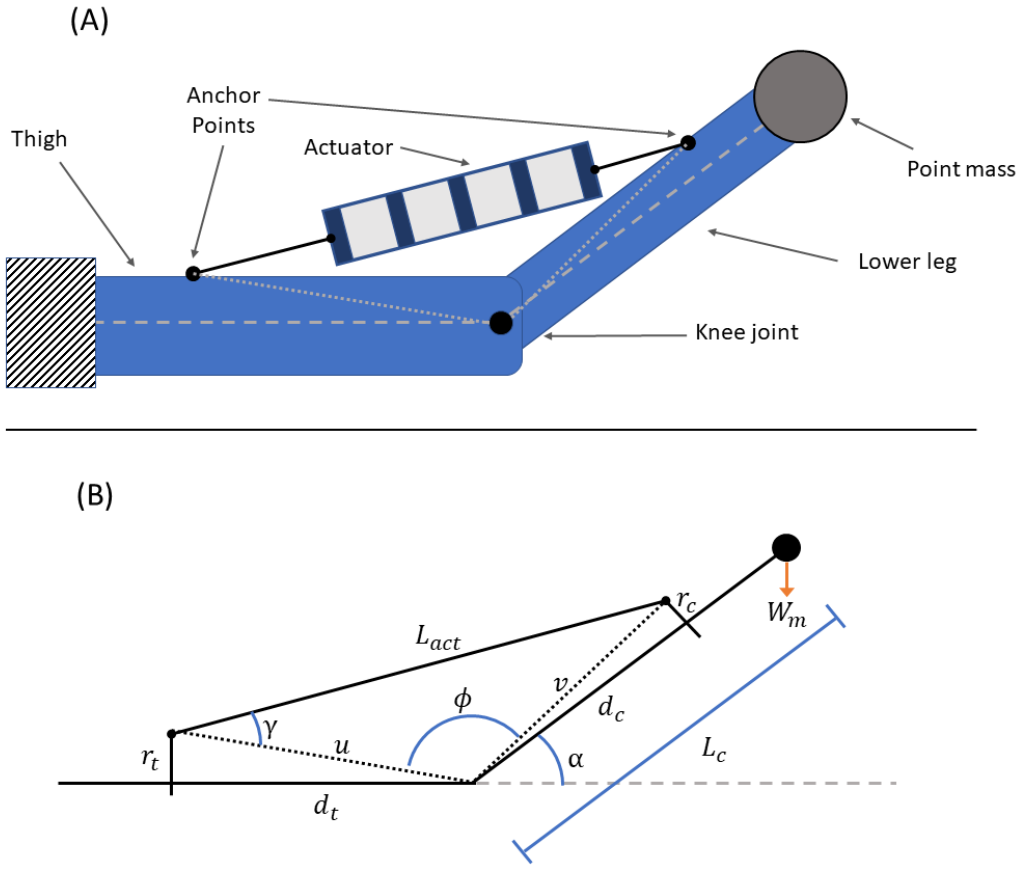

Figure 4-1: Schematic of simplified leg proxy flexion exoskeleton, showing (A) the layout of the components, and (B) the diagram for a simple quasi-static model of the system, labelling the geometrical sections of the leg and the weight of the point mass at the end. Greek letters correspond to angles, "t" subscript to thigh, "c" subscript to lower leg, and "act" for actuator.

effects of a Spina-Bifida-related immobility on joint range and limb development, the case study simulates the use of a soft-actuated exoskeleton for flexing an infant's leg from the prone position. Figure 4-1 shows the setup, where an actuator is placed across two rigid beams serving as the fixed "thigh" and rotating "lower leg". A 200g mass was placed at the end of the "lower leg," to approximate the weight of the leg of a 6-month old child.

4.2 Modelling the Case Study System

To analyze this system, one can make a quasi-static assumption, where the output force of the actuator causes a torque about the knee joint equal and opposite to the torque generated

by the point mass at the end of the lower leg beam. From this assumption, one can find the required output force of the actuator for all angles of the leg during flexion for a given angle of the leg. Additionally, the contraction of the actuator (non-scaled) can be found by subtracting the distance between the two actuator anchor points at any angle from their distance initial distance – when the leg is in the extended configuration ($\alpha = 15^o$). The equations below describe the process for calculating the required force and contraction for a given angle, α of the leg with the horizontal. All variables are labeled in Figure 4-1.

$$\phi = \pi - \alpha - \tan^{-1}\left(\frac{r_c}{d_c}\right) - \tan^{-1}\left(\frac{r_t}{d_t}\right)$$
$$u = \sqrt{r_t^2 + d_t^2} \quad ; \quad v = \sqrt{r_c^2 + d_c^2}$$
$$L_{act} = \sqrt{u^2 + v^2 - 2\,u\,v\cos(\phi)}$$
$$\gamma = \sin^{-1}\left(\frac{v * \sin(\phi)}{L_{act}}\right)$$

$$F_{req} = \frac{Wm\, L_c \mathbf{cos}(\alpha)}{u * \mathbf{sin}(\gamma)} \tag{4.1}$$

$$c_{req} = L_{act}(\alpha = \mathbf{0}^o) - L_{act}(\alpha) \tag{4.2}$$

Combining the required actuator force and its contraction, one can generate a required FCP for the vacuum actuator that serves as a reference for actuator design. Figure 4-2 shows the required force-contraction curve for this system when the anchoring points are at the base of the thigh and middle of the lower leg. From this, it is important to note that the actuator force is high at the zero-contraction point and quickly drops during contraction, matching the trend for the FCP of a bellows actuator.

In this case study, the actuator chosen is a bellows actuator with a rectangular cross section of 15x30mm and an R of 1 with six contractile cells (see Figure 4-3). This gives it a total length of 110mm and a contractile length (length excluding the thickness of its rings) of 90mm. Given the contraction extracted from the leg proxy model is 75mm, this translates to the actuator undergoing contraction of 83%. The R=1 means the gap between the rings is equal to the smaller dimension of the rectangle, 15mm – FEM models were performed to confirm that the gap ratio, R, is dominated by the smaller radial dimension of the cross-section (see Appendix, Figure A-4) . A rectangular shape was chosen for

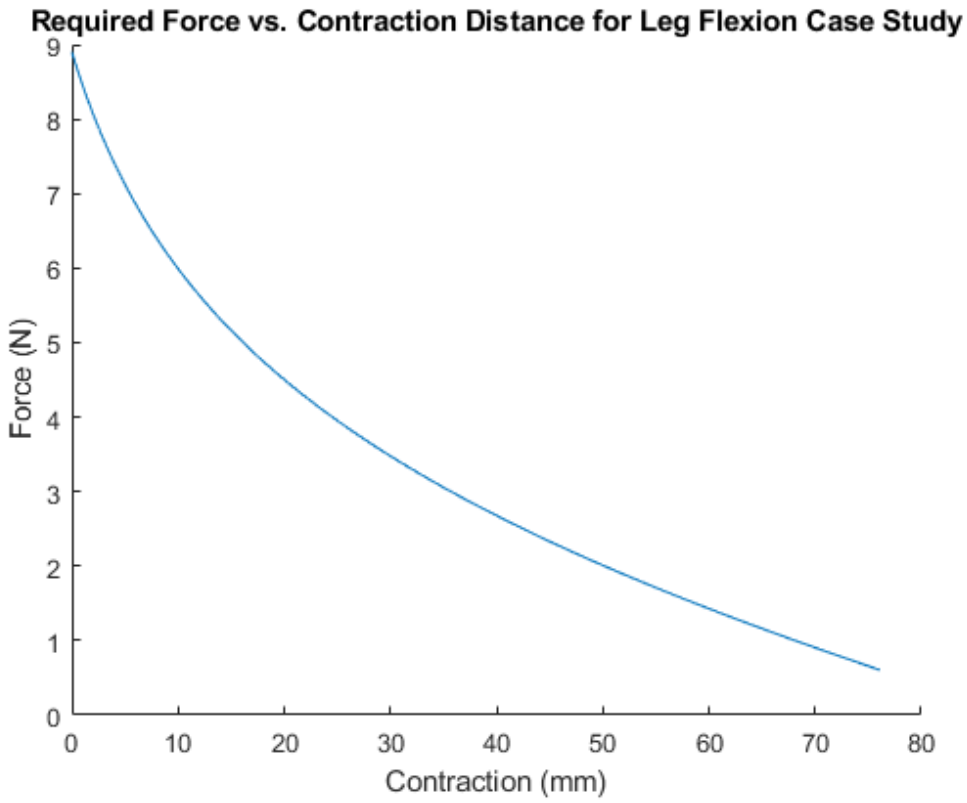

Figure 4-2: Required FCP of actuator assuming a quasi-static system in the simplified leg proxy model, calculating the required actuator tension to maintain a quasi-static state for a given value of the leg angle, α.

this actuator due to simplified manufacturing as well as the possibility of an actuator with a lower profile, more closely conforming to the body. FEM models were performed to confirm that the gap ratio, R, of a non-circular bellows actuator is dominated by the smaller dimension of the cross-section.

4.2.1 Applying the FEM and Virtual Work Models to the System

To assess the use of the virtual work model in a design scenario, we predicted the actuation input pressures necessary to contract the leg proxy in a quasi-static manner. This would give designers a sense of the practical pneumatic capabilities that would be required of their engineered system, and what kind of control scheme would be necessary. To predict the required input pressure, we use the linear relationship between pressure and output force used in the piston-scaling scheme of the virtual work model. This is done by multiplying the piston-scaled force output of the model by the actuator's cross-sectional area, to find a force-per-unit-pressure of the actuator. Finally, by dividing the force required by the actuator calculated from the leg proxy model, one can find the required pressure value throughout the actuator's contraction, see Equation 4.3 below:

$$P_{req}(x) = \frac{F_{req}(x)}{F^*_{actuator}(x) * A_c} \tag{4.3}$$

To apply the appropriate scaling factor to the value of $F^*_{actuator}$ from the virtual work model, we performed a set of tensile tests of the 0.125mm thickness polyethylene film used as the skin material used to construct the actuator. The transverse and longitudinal stiffnesses varied from each other by 30% (81MPa longitudinal vs. 130MPa for transverse), but the average was chosen – 110MPa. Using these values for Young's Modulus and thickness, we found a scaling factor of 0.48 to be applied.

To further compare the accuracy of the Virtual Work model with a baseline, we recreated an FEM version of the actuator in this case study, using the same method as was used to model bellows actuators, changing the cross-section to 30x15mm, skin thickness to 0.125mm, and Young's Modulus to 110MPa. The actuation pressure was also raised to 15kPa, so the model would operate at a closer range to the magnitudes predicted for the

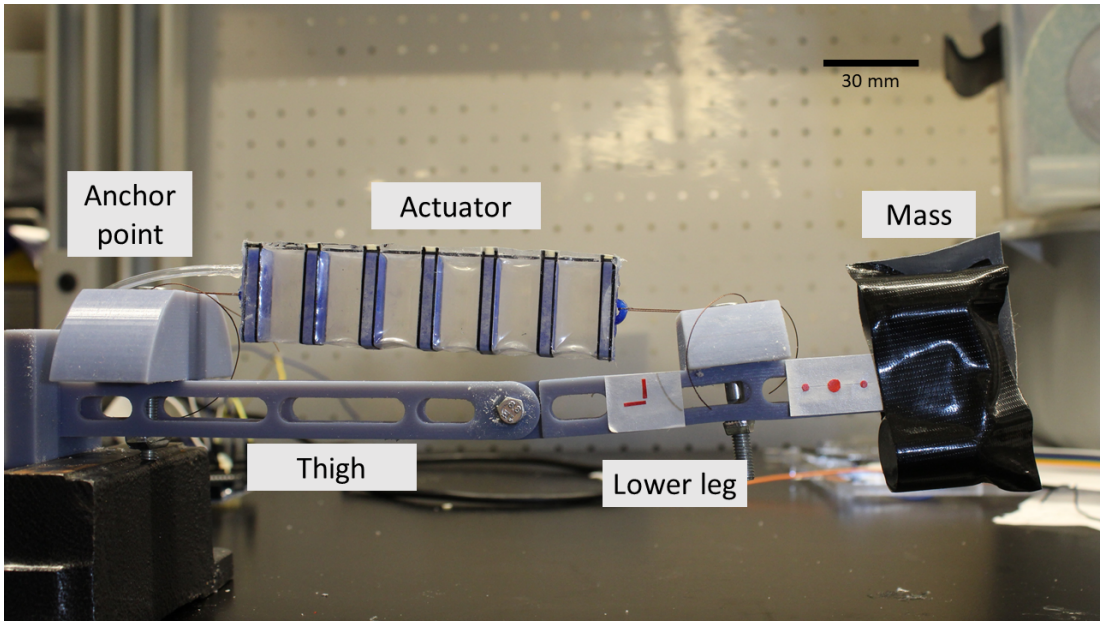

Figure 4-3: Picture of leg proxy setup with labels for the major components. Markers for image processing can be seen on lower leg piece. Actuator attached to bolts on anchoring blocks (not visible) with thread, and a 1/16" ID tube used to connect actuator to vacuum source.

application. The FCP from the FEM model was extracted, scaled, and the same process was applied to it.

4.3 Experimental Methods and Results

4.3.1 Methods

To assess the accuracy of the modelling approach to predict the quasi-static pressures for the leg proxy flexion, an experimental setup was built, as shown in Figure 4-3. A fixed thigh beam and a rotating lower leg beam were 3D printed (Object 30 Prime), with slots to allow the affixing of anchoring blocks at varying positions. Anchoring blocks serve as attachment points for the actuator and have radii matching corresponding portions of the infant leg. The thigh anchor was placed on a 35mm-radius anchor block at 120mm from the knee joint, and the lower leg anchor was on a 25mm-radius anchor block 70mm from the knee. The 200g mass at 130mm from the knee was attached to the end of the lower leg beam piece, using two separate 100g calibrated weights to ensure the center of gravity

of the mass matched the center line of the leg. The actuator was affixed to the anchoring points through two loops placed at the ends of the actuator, which were tied to the bolts on the anchor blocks.

To control the input pressure, a manual vacuum gauge (IRV10-N07, SMC) was connected in series to the actuator, and a TruWave pressure sensor (Edwards Lifesciences) was used to monitor the true pressure input during the experiment. A digital camera (Nikon D3400) was placed level with the thigh, centered on the knee joint, and markers were placed on the lower leg to allow image tracking.

The experiment was performed by setting the desired pressure with the manual gauge and waiting for the leg to flex and reach equilibrium. Once equilibrium was achieved (no motion of the leg), the pressure reading from the sensor was recorded, and a picture was captured. The process was repeated in small pressure increments (approximately 1kPa) until the leg no longer stopped at equilibrium without contracting fully. This signaled the "maximum pressure point", where subsequent angles of leg flexion required decreasing pressure inputs (this can be seen particularly in Figure 4-4 for the FEM model, where there is a visible maximum pressure)

4.3.2 Results and Discussion

The results of the experiment compared to the scaled Virtual Work and FEM model predictions are included below in Figure 4-4.

As can be seen in Figure 4-4, the input pressure magnitude range predicted by the models (10-19kPa) match the experimental results closely. The parabolic shape of the pressure curve is echoed in all models, though there is a divergence in similarity between curve slope, particularly in the less pronounced slope of the virtual work model slope. Despite this, both the virtual work and FEM models predict the maximum pressure point to close accuracy. In terms of angle, the experimental value is $37^o \pm 1^o$, while the value predicted by the virtual work and FEM models were 31.8^o and 37.0^o respectively, corresponding to an error of 15% and 1% . For the pressure magnitude, the virtual work model had an error of 9% and the FEM model one of 5%.

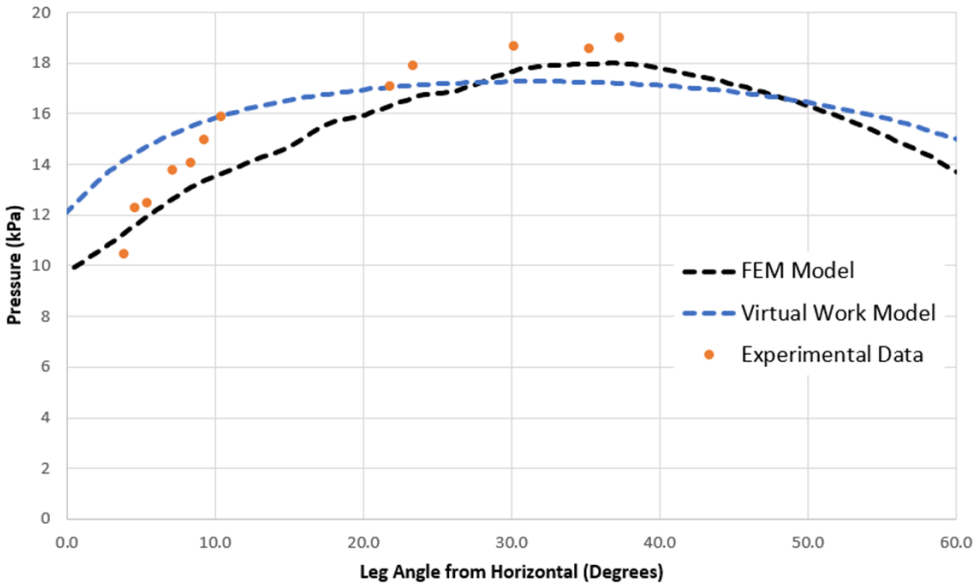

Figure 4-4: Results of quasi-static leg experiment, comparing input pressure for equilibrium leg angle (α). Overlaid with predicted pressure curve from an FEM model of the actuator (30x15mm cross section, R=1, skin E = 106MPa and thickness = 0.125mm) and the scaled virtual work model.

4.4 Conclusion

As this case study demonstrated, the virtual work model can be applied to application-specific models to aid in the prediction of relevant parameters, such as required pressure output and give the user of the tool an initial sense of the complexity of the pressure control required for an application. With an accuracy in the range of 15%, it is a sufficient model for the early stages of design screening and iteration. Due to its rapid ability to solve for actuator FCPs, the model can also be used to perform larger parameter sweeps of different actuator geometries and optimize for certain parameters in the application. In this case, this might come in the form of maximizing the initial contraction force, finding an actuator with maximum contraction matching the desired flexion angle range, or placing certain constraints on the pressure control curve, such as finding the most constant curve. Future work pertaining to application-specific modelling would include a platform for rapid construction of simplified application models and actuator loading conditions, to streamline the process further.

Chapter 5

Discussion and Conclusions from Modelling Work

5.1 Discussion

5.1.1 Bellows Actuator – Model and Experimental Results Comparison

In our work, the bellows actuator was chosen as the first application as its simple design allows it to be realistically idealized by the assumptions made in the model, without the need for additional components. In Figure 3-2, we demonstrate that the model can predict FCPs with varying gaps as well as performing large parameter sweeps with high granularity. Our findings are consistent with the major trends found in the analytical model from Felt et al. (2018). Namely by increasing R, the force magnitude on the initial part of the contraction is increased while the total stroke is decreased for an R above 1. Additionally, the smaller the value of R the more constant the FCP becomes. The heat map in Figure 3-2B also agrees closely with that in Felt et al. (2018) and can give users a holistic view of the design space and help inform the actuator selection process (see Figure 5-1 and Chapter 4). As can be seen in Figure 5-1, the models are in close agreement – the estimated contraction lengths, the trend of force distribution are similar, though the Felt model implemented a more complex skin profile function which is a strong possible reason for the discrepancy

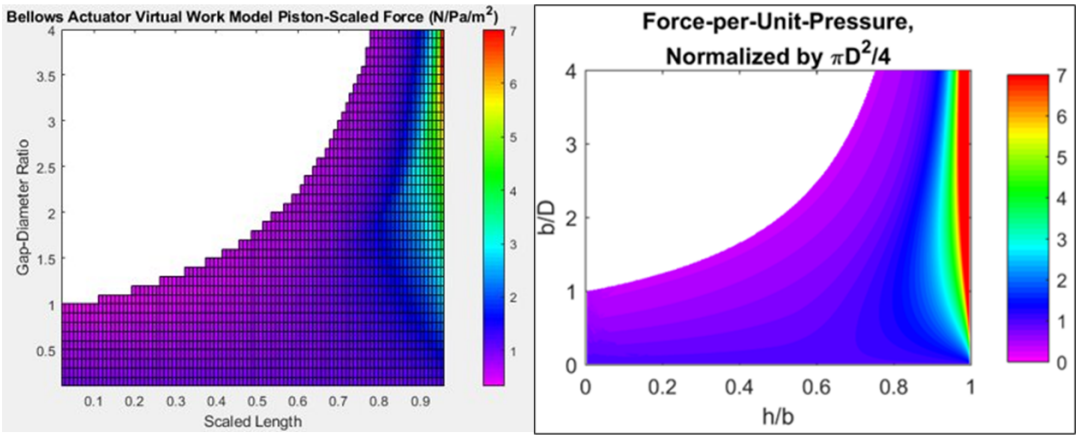

Figure 5-1: Comparison of our parameter sweep (Left) of FCPs for bellows actuators of different values of R with Felt et al. 2018 (Right). Color scale corresponds to force magnitude. Though there is some deviation, the contraction limits and general magnitude trends match – differences may be due to Felt's use of a different skin function.[1]

in scaled force magnitudes.

Comparing the model and experimental results in Figure 3-6, we observe a close agreement in terms of FCP. During the early phase of the contraction, particularly for the R = 0.5 and 1 sets, there is close agreement but we see some deviation of the modeling results from the experimental results towards the end of contraction in all cases for bellows actuators (Figure 3-6), most likely due to the zero-thickness skin and zero-energy-loss assumption in the virtual work model. With these assumptions, the skin collapses in an orderly fashion until the cell contraction reaches 100%, when in reality the thickness and complex crumpling mechanics of the skin causes a nonlinear restoring force that increases towards the end of the contraction, as demonstrated in the compression testing for bellows actuators in Chapter 3. This phenomenon of a nonlinear decreasing force is corroborated in the experimental results from Felt et al. (2018).

By overlaying the measured restoring force of each bellows actuator with the model for individual actuators, the output curve is estimated more closely (Figure A-3). The FCP curves downward at the end of the contraction, matching the trend seen experimentally, and

the final contraction is more closely approximated (with an average error of 14%). Given the complex mechanics of this crumpling skin restoring force, future work would be needed to create a predictable model based on this phenomenon. The effect of a restoring spring force is further investigated in our FOAM model, where the skeleton's restoring force is characterized by a linear trend.

5.1.2 FOAM Actuator – Model and Experimental Results Comparison

Comparing the FOAMs parameter sweep figure (Figure 3-3) with the results see in Figure 3-2, we can see the same general trend is preserved, where there are higher forces and lower maximum contraction with increasing . One key difference from the results for the bellows actuators is demonstrated by the = 90o case, where the maximum contraction is restricted by the force magnitude reaching zero. This means the radial volume loss reaches a maximum, leading the derivative to reach zero, unlike for the bellows actuator where maximum contraction is bounded by a geometrical constraint when the skin collapses fully against the boundary. This demonstrates the importance of defining specific boundary functions in the virtual work model, based on actuator design.

As hypothesized, Figure 2-6 illustrates the importance of including the skeleton spring force in the model for predicting the FOAM force profile. Though the initial FCP from the pure virtual work model matches that of the FEM, once the spring force becomes non-negligible, the virtual work model deviates and predicts much higher force and contraction at the end of the FCP that what is predicted by the model. The results of excluding a spring force in the model are two-fold; an over-estimated contraction distance and a larger force profile towards the end section. The results also show that the spring force can be subtracted linearly as a post-processing step, rather than having to be integrated into the virtual work model framework itself.

In keeping with this demonstration, the experimental results in Figure 3-7 show that the virtual work model with the subtracted skeleton spring force can closely predict the FOAM actuator force profile. In the case of = 30o, the experimental contraction is smaller

compared to our prediction. This indicates that the spring resistance force from the skeleton may contribute less when the absolute displacement of the skeleton is smaller (because the 30-degree skeleton is comparatively shorter than the others). In this case, similar to the bellows actuator, the loss may be dominated by the skin's restoring force, which is not captured in this model.

5.1.3 Generalizing Model to Other Actuator Designs

As initially explained, this model is ideally applied to skin-skeleton actuators, as it assumes a thin inextensible film being pulled towards a skeleton or boundary with a vacuum, and additional components can be added to account for the material of the skin and the system's restoring force. From these two examples, we have demonstrated the model's ability to be applied to different actuator geometries and its modularity in combining with external models. With these conclusions in mind, the model can be applied to other more mechanically complex actuator designs, and we list some examples in this section.

The vacuum-powered curling actuator in Tawk et al. 2018 has the necessary thin skin and skeleton components, though it does not undergo linear contraction. Figure 5-2 shows how the skin and boundary functions can be applied, with the boundary function changing during contraction to accommodate for the contractile cell's bending. The output linear force can be converted to a torque by assuming a point load at the half-way height or other more complex force distributions along the height. A cantilever-based torsional spring model would also be overlaid to account for the restoring force of the bending skeleton.

Another possible application would be the buckling actuators in Yang et al. 2016 (Figure 5-2). The key issue in this case is the skin is a proportionally thick elastomeric layer, which may still allow for the inextensible assumption, but not that of a thin-film. A virtual thickness must be included in the model to account for the limitation on the stroke length, and a more complex spring model based on buckling would be included to model the skin's restoring force. In that case, parameters such as skin thickness and material would be interesting to modulate, in addition to the usual contractile cell length and aspect ratio .

A process such as this – defining the skin and skeleton profile functions, reassessing

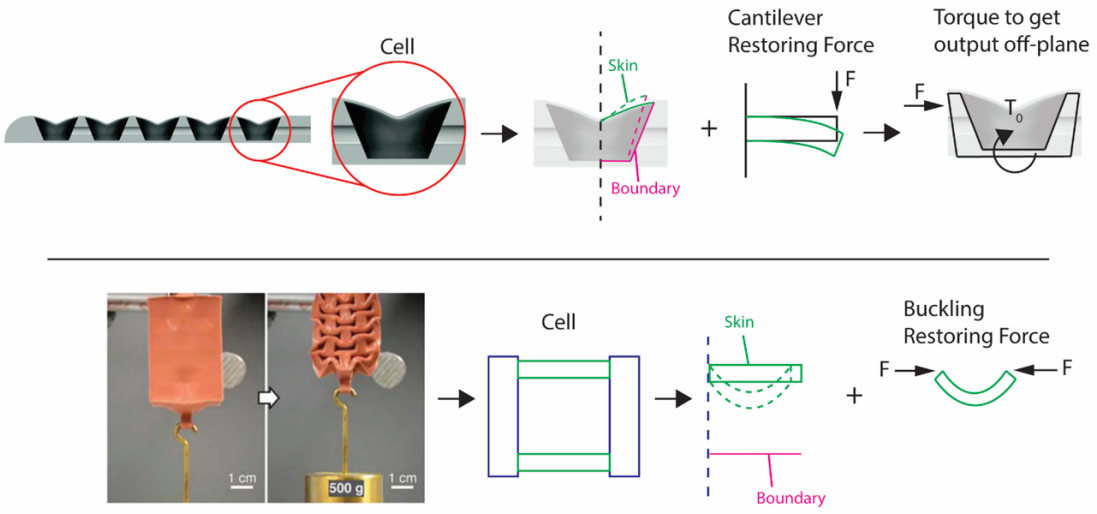

Figure 5-2: Schematic of how our model may be applied to different more complex actuators, such as a curling actuator [22] and a buckling elastomeric actuator [25]. As described, the basic steps include (1) defining the cell geometry (2) defining skin and boundary functions (3) establishing additional external components to compensate for infinite-stiffness and zero-loss assumptions of mode.[1]

the base model's assumptions, and defining additional restoring force or loss components to overlay into model – can be repeated for other actuators that fall under the vacuum powered skin-skeleton category of actuators.

As a final note on further generalizability - the power of the virtual work principle is the computational simplicity in reaching an accurate estimate of a vacuum actuator's force-contraction profile. This implies a possible approach to actuator design for more complex FCPs by controlling the volume loss rate. Actuators with origami skin patterns[28, 21, 13], for example, have high potential in this application, as a new model could be developed and use the geometrical predictability of origami to generate new actuator designs to fit desired force-profiles.

5.1.4 Limitations

In addition to illustrating the concept of virtual work, the curve in Figure 3-1 also illustrates one of the limitations of the model: the large initial force. This large force is due to the

assumption that the skin at zero contraction is in full tension. In any practical implementation of an actuator, this does not hold for multiple reasons. First, there is often a small tolerance between the skin and the actuator skeleton, or in the case of the bellows actuator where there is no gap, asymmetries in the construction can lead to sections of the skin that are not in perfect tension. Perhaps more importantly, this assumption conflicts with the quasi-static nature of the system, as the pressure applies a radially-oriented (perpendicular) force on the skin that can only be compensated for by the tension on the skin [21], requiring some initial curvature to allow for a radial component of the tension force. The effect of this physical inaccuracy is that, when comparing with experimental data, it is important to shift the model horizontally towards the negative x direction by some small percentage to eliminate the high peak force. After implementing a scaling factor that considers the above logic about a required initial skin curvature, the initial peak force was still higher than the experimental case, most probably due to the other flaws of fabrication that lead to an initial curvature in the skin. Given these unquantifiable factors, a shifting factor of 2% was implemented. This means in all comparisons of the model FCP with experimental data, the model FCP is shifted horizontally so its zero-point begins at a contraction of 2%.

In Figure 3-6, for the bellows with an R of 2, the model overpredicts the output force most probably due to this tension phenomenon. The large unsupported length of skin may have experienced higher cumulative pressure force and larger tension force compared to R = 0.5, 1, (as supported by the higher peak force for R = 2 in Figure 3-2A). This means the initial sagging of the skin for R = 2 may be greater than for 0.5 and 1, calling for a larger shift. Shifting the model by 2% for R = 2 eliminates the larger error in the estimated initial force and better approximates the early phase of the force profile.

Finally, in Figure 3-3, there is a consistent over-estimation of the initial force. We hypothesize that this is a result of the aforementioned tension phenomenon combined with the fact that the skin in FOAMs, unlike for bellows actuators, is not directly anchored to the skeleton, implying that the sections of skin between the skeleton are slightly longer than the ideal perfect-tension model predicts. Due to the overall similarity in the profile shape, there is a better agreement with experimental results if the model is further shifted horizontally in this case as well.

5.2 Conclusion

In this work, we hypothesized that the nonlinear force-contraction profile of a skin-skeleton vacuum actuator can be derived purely from a geometrical calculation of its volume loss rate. We tested this with the model and experiments presented here and proved that our hypothesis was valid. Though the magnitudes of the resultant forces are dependent on external properties, such as skin material, skeleton and skin restoring forces, and actuation pressure, we show that the shape of the FCP is dominated by the work done through volume loss rate. By applying the piston-scaled force and scaling factor and overlaying external models to capture the system's restoring force, we can closely estimate the output of different actuators with much less computational and set-up time than developing actuator-specific FEM or analytical models. Importantly, these external models can be separately super-imposed on the FCP calculated by the virtual work model, preserving its modularity. Inaccuracies in this model are compensated for by its generalizability and utility as a design guiding tool to allow rapid parameter space sweeps. Furthermore, these rapid parameter variations can be used to estimate application-specific values, such as actuation pressure range and the expected pressure control scheme, as was demonstrated in the leg flexion case study.

Future work would include developing a more robust system of modules that can model the restoring forces for various skin and skeleton geometries to interface with the virtual work model, as this is currently one of the largest sources of discrepancy between the model and experimental data. More work can also be done on understanding the effect of the skin material on the output force magnitude.

Notwithstanding these challenges, the generalized and modular nature of this framework enables its implementation as a design tool for a wide variety of vacuum actuators, provided they can be represented by one or more simplified skin-skeleton contraction cells. This ability to rapidly model a variety of actuators and actuator geometrical parameters has broad implications in improving design efficiency and speed in the fields of medical devices, robotics, and soft machines. For example, it can enable actuator design for application-specific force profiles, such as in patient-specific devices or robotic design, and the rapid computational time can be useful for dynamic closed-loop control applications in

diverse soft robotic applications.

Bibliography

[1] Samuel Dutra Gollob, Clara Park, Bon Ho Brandon Koo, and Ellen T. Roche. A Modular Geometrical Framework for Modelling the Force-Contraction Profile of Vacuum-Powered Soft Actuators. *Frontiers in Robotics and AI*, 8:15, mar 2021.

[2] Daniela Rus and Michael T. Tolley. Design, fabrication and control of soft robots, may 2015.

[3] Sangbae Kim, Elliot Hawkes, Kyujin Cho, Matthew Jolda, Joe Foley, and Robert Wood. Micro artificial muscle fiber using NiTi spring for soft robotics. In *2009 IEEE/RSJ International Conference on Intelligent Robots and Systems, IROS 2009*, pages 2228–2234, dec 2009.

[4] M. Calisti, M. Giorelli, G. Levy, B. Mazzolai, B. Hochner, C. Laschi, and P. Dario. An octopus-bioinspired solution to movement and manipulation for soft robots. *Bioinspiration and Biomimetics*, 6(3):036002, jun 2011.

[5] Aslan Miriyev, Kenneth Stack, and Hod Lipson. Soft material for soft actuators. *Nature Communications*, 8(1):1–8, dec 2017.

[6] Benjamin C. Mac Murray, Chaim C. Futran, Jeanne Lee, Kevin W. O'Brien, Amir A. Amiri Moghadam, Bobak Mosadegh, Meredith N. Silberstein, James K. Min, and Robert F. Shepherd. Compliant Buckled Foam Actuators and Application in Patient-Specific Direct Cardiac Compression. *Soft Robotics*, 5(1):99–108, feb 2018.

[7] Ellen T. Roche, Markus A. Horvath, Isaac Wamala, Ali Alazmani, Sang Eun Song, William Whyte, Zurab Machaidze, Christopher J. Payne, James C. Weaver, Gregory Fishbein, Joseph Kuebler, Nikolay V. Vasilyev, David J. Mooney, Frank A. Pigula, and Conor J. Walsh. Soft robotic sleeve supports heart function. *Science Translational Medicine*, 9(373), jan 2017.

[8] Panagiotis Polygerinos, Kevin C. Galloway, Emily Savage, Maxwell Herman, Kathleen O'Donnell, and Conor J. Walsh. Soft robotic glove for hand rehabilitation and task specific training. In *Proceedings - IEEE International Conference on Robotics and Automation*, volume 2015-June, pages 2913–2919. Institute of Electrical and Electronics Engineers Inc., jun 2015.

[9] Allison P. Porter, Barnaba Marchesini, Irina Potryasilova, Enrico Rossetto, and Dava J. Newman. Soft Exoskeleton Knee Prototype for Advanced Space Suits and

Planetary Exploration. pages 1–13. Institute of Electrical and Electronics Engineers (IEEE), aug 2020.

[10] Georgios Andrikopoulos, Georgios Nikolakopoulos, and Stamatis Manesis. A Survey on applications of Pneumatic Artificial Muscles. In *2011 19th Mediterranean Conference on Control and Automation, MED 2011*, pages 1439–1446, 2011.

[11] Keiko Ogura, Shuichi Wakimoto, Koichi Suzumori, and Yasutaka Nishioka. Micro pneumatic curling actuator - Nematode actuator -. pages 462–467. Institute of Electrical and Electronics Engineers (IEEE), jun 2009.

[12] Robert K. Katzschmann, Andrew D. Marchese, and Daniela Rus. Hydraulic autonomous soft robotic fish for 3D swimming. In *Springer Tracts in Advanced Robotics*, volume 109, pages 405–420. Springer Verlag, 2016.

[13] Ramses V. Martinez, Carina R. Fish, Xin Chen, and George M. Whitesides. Elastomeric Origami: Programmable Paper-Elastomer Composites as Pneumatic Actuators. *Advanced Functional Materials*, 22(7):1376–1384, apr 2012.

[14] Bobak Mosadegh, Panagiotis Polygerinos, Christoph Keplinger, Sophia Wennstedt, Robert F. Shepherd, Unmukt Gupta, Jongmin Shim, Katia Bertoldi, Conor J. Walsh, and George M. Whitesides. Pneumatic networks for soft robotics that actuate rapidly. *Advanced Functional Materials*, 24(15):2163–2170, apr 2014.

[15] Raphael Deimel and Oliver Brock. A novel type of compliant and underactuated robotic hand for dexterous grasping. *International Journal of Robotics Research*, 35(1-3):161–185, jan 2016.

[16] Fionnuala Connolly, Panagiotis Polygerinos, Conor J. Walsh, and Katia Bertoldi. Mechanical programming of soft actuators by varying fiber angle. *Soft Robotics*, 2(1):26–32, mar 2015.

[17] Jackson Wirekoh and Yong Lae Park. Design of flat pneumatic artificial muscles. *Smart Materials and Structures*, 26(3):035009, feb 2017.

[18] Ching Ping Chou and Blake Hannaford. Measurement and modeling of McKibben pneumatic artificial muscles. *IEEE Transactions on Robotics and Automation*, 12(1):90–102, 1996.

[19] Siddharth Sanan, Peter S. Lynn, and Saul T. Griffith. Pneumatic torsional actuators for inflatable robots. *Journal of Mechanisms and Robotics*, 6(3), apr 2014.

[20] Ryuma Niiyama, Xu Sun, Cynthia Sung, Byoungkwon An, Daniela Rus, and Sangbae Kim. Pouch motors: Printable soft actuators integrated with computational design. *Soft Robotics*, 2(2):59–70, jun 2015.

[21] Shuguang Li, Daniel M. Vogt, Daniela Rus, and Robert J. Wood. Fluid-driven origami-inspired artificial muscles. *PNAS*, 114(50):13132–13137, 2017.

[22] Charbel Tawk, Marc In Het Panhuis, Geoffrey M. Spinks, and Gursel Alici. Bioinspired 3d printable soft vacuum actuators for locomotion robots, grippers and artificial muscles. *Soft Robotics*, 5(6):685–694, dec 2018.

[23] Matthew A. Robertson and Jamie Paik. Low-inertia vacuum-powered soft pneumatic actuator coil characterization and design methodology. In *2018 IEEE International Conference on Soft Robotics, RoboSoft 2018*, pages 431–436. Institute of Electrical and Electronics Engineers Inc., jul 2018.

[24] Dian Yang, Mohit S. Verma, Elton Lossner, Duncan Stothers, and George M. Whitesides. Negative-Pressure Soft Linear Actuator with a Mechanical Advantage. *Advanced Materials Technologies*, 2(1):1600164, jan 2017.

[25] Dian Yang, Mohit S Verma, Ju-Hee So, Bobak Mosadegh, Christoph Keplinger, Benjamin Lee, Fatemeh Khashai, Elton Lossner, Zhigang Suo, George M Whitesides, D Yang, M S Verma, J-h So, B Mosadegh, C Keplinger, B Lee, F Khashai, E Lossner, G M Whitesides, and Z Suo. Buckling Pneumatic Linear Actuators Inspired by Muscle. *Advanced Materials Technologies*, 2016.

[26] Shuguang Li, Richa Batra, David Brown, Hyun Dong Chang, Nikhil Ranganathan, Chuck Hoberman, Daniela Rus, and Hod Lipson. Particle robotics based on statistical mechanics of loosely coupled components, mar 2019.

[27] Wyatt Felt, Matthew A. Robertson, and Jamie Paik. Modeling vacuum bellows soft pneumatic actuators with optimal mechanical performance. In *2018 IEEE International Conference on Soft Robotics, RoboSoft 2018*, pages 534–540. Institute of Electrical and Electronics Engineers Inc., jul 2018.

[28] Jin Gyu Lee and Hugo Rodrigue. Origami-Based Vacuum Pneumatic Artificial Muscles with Large Contraction Ratios. *Soft Robotics*, 6(1):109–117, feb 2019.

[29] Zhongdong Jiao, Chen Ji, Jun Zou, Huayong Yang, and Min Pan. Vacuum-Powered Soft Pneumatic Twisting Actuators to Empower New Capabilities for Soft Robots. *Advanced Materials Technologies*, 4(1):1800429, jan 2019.

[30] Gunjan Agarwal, Matthew A. Robertson, Harshal Sonar, and Jamie Paik. Design and Computational Modeling of a Modular, Compliant Robotic Assembly for Human Lumbar Unit and Spinal Cord Assistance. *Scientific Reports*, 7(1), dec 2017.

[31] Cosima du Pasquier, Tian Chen, Skylar Tibbits, and Kristina Shea. Design and Computational Modeling of a 3D Printed Pneumatic Toolkit for Soft Robotics. *Soft Robotics*, 6(5):657–663, oct 2019.

[32] Pham Huy Nguyen and Wenlong Zhang. Design and Computational Modeling of Fabric Soft Pneumatic Actuators for Wearable Assistive Devices. *Scientific Reports*, 10(1):66, dec 2020.

[33] Panagiotis Polygerinos, Zheng Wang, Johannes T.B. Overvelde, Kevin C. Galloway, Robert J. Wood, Katia Bertoldi, and Conor J. Walsh. Modeling of Soft Fiber-Reinforced Bending Actuators. *IEEE Transactions on Robotics*, 31(3):778–789, jun 2015.

[34] Warren C. Young and Richard G. Budynas. *Roark's Formulas for Stress and Strain*. 2002.

[35] Spina Bifida Fact Sheet. National Institute of Neurological Disorders and Stroke.

[36] Spina Bifida Occulta. Physiopedia.com.

[37] Elena Tappit-Emas. Spina Bifida. In *Pediatric Physical Therapy*, pages 231–280. Wolters Kluwer & Lippincott Williams and Wilkins, Phyladephia, 4th edition. original-date: 2008.

Appendix A

Supplementary Figures

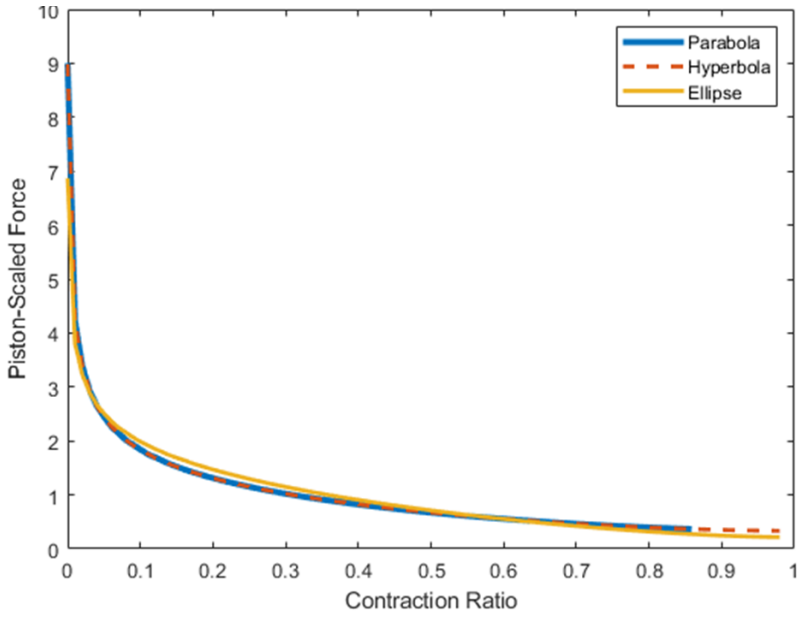

Figure A-1: Force contraction profile for bellows actuators with varying skin profile functions using different conical sections, for gap ratio R = 1. One can see the similarity despite the different skin functions, showing that using any simple conical section leads to similar results.

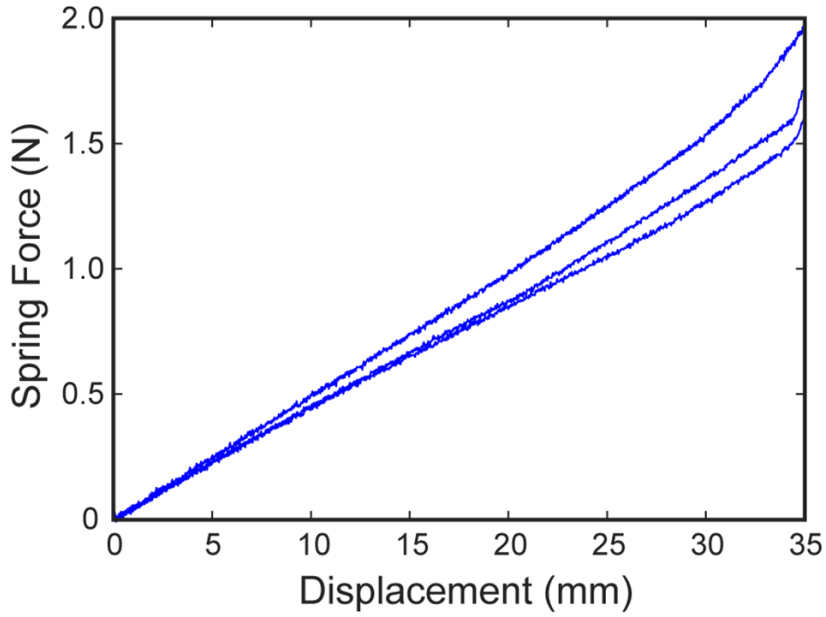

Figure A-2: Measured spring force from 30-degree zigzag skeletons during a compression test (n=3). Average linear stiffness extracted from these three experiments was used as the spring stiffness of the FOAM skeleton for super-imposing with the virtual work model.

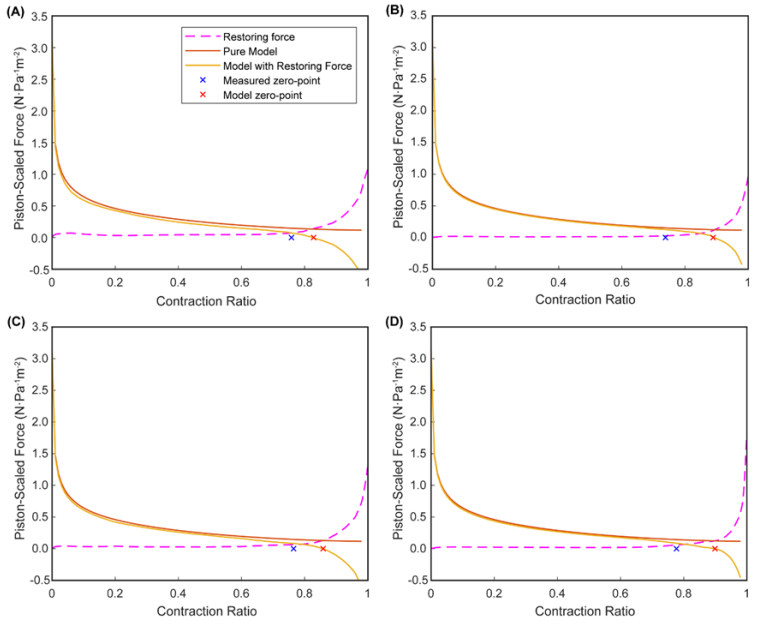

Figure A-3: Results of empty bellows actuator compression experiments ("Restoring force") overlaid on model-predicted FCP ("Pure Model"). Measured zero-point corresponds to value measured from compression experiment, while model zero-point corresponds to that predicted by the overlaid model ("Model with Restoring Force"). An average of 14% error between measured and modelled end of contraction is seen. (A)-(D) are the four replicates for bellows actuators for R=1.

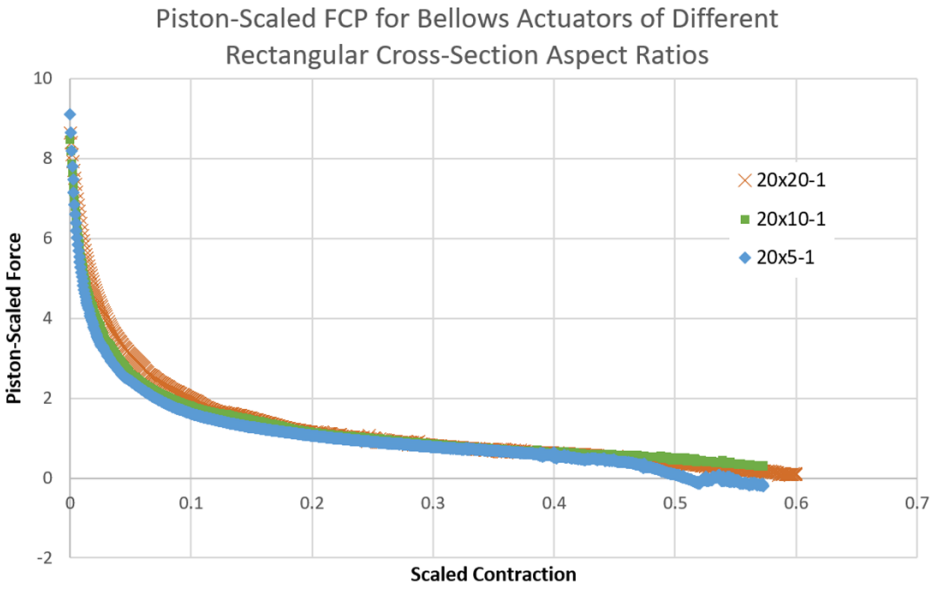

Figure A-4: Piston-Scaled FCPs of rectangular bellows actuators from FEM models with varying cross-sectional area dimensions, where graph legends are of the format (WxH-R). This shows that even though the actuators had different lengths and output force magnitudes, once their output was scaled by cross-sectional area and pressure, and their contraction scaled by length, their FCPs followed the same trend, defined by the value of R. R is relative to the smallest dimension, for example, in the 20x10mm cross section case, an R=1 corresponds to a gap between rings of 10mm.